Diketopyrrolo[3,4-c]pyrrole derivative as a promising ligand for the stabilization of G-quadruplex DNA structures

Catarina I. V. Ramos[1],*, Vitor A. S. Almodôvar[1], Nuno Candeias[1,2], Tiago Santos[3], Carla Cruz[3],*, M. Graça P. M. S. Neves[1] and Augusto C. Tomé[1],*

[1] LAQV-REQUIMTE, Department of Chemistry, University of Aveiro, 3810-193 Aveiro, Portugal
[2] Faculty of Engineering and Natural Sciences, Tampere University, Korkeakoulunkatu 8, 33101 Tampere, Finland
[3] CICS-UBI - Centro de Investigação em Ciências da Saúde, Universidade da Beira Interior, Av. Infante D. Henrique, 6200-506, Covilhã, Portugal
* Correspondence: c.ramos@ua.pt; carlacruz@fcsaude.ubi.pt; actome@ua.pt

Abstract

Telomerase, oncogenes and tumor suppressors are closely associated with tumour occurrence, therefore these structures are being recognized as targets for the development of new anticancer drugs.

The efficacy of several molecules in telomerase inhibition and regulation of genes expression, by adduct formation with G-quadruplexes (G4), has been studied by biophysical and biochemical methods with promising results. We report here the synthesis and structural characterization of a small positively charged diketopyrrolo[3,4-*c*]pyrrole derivative, identified as DPP(PyMe)$_2$, that showed very promising results as G4 stabilizing ligand.

The data obtained from UV-Vis and fluorescence experiments suggest that DPP(PyMe)$_2$ presents high affinity to G4 structures. Docking studies and molecular dynamics simulations unraveled the binding modes of the ligand with four G4 structures. The obtained results also allowed us to conclude that the DPP(PyMe)$_2$ ligand binds into the top G-tetrad or in a mixed binding mode depending on the GQ structure.

A remarkable selectivity of DPP(PyMe)$_2$ for c-MYC and KRAS 32R in the presence of ds26 was observed by circular dichroism (CD) and fluorescence resonance energy transfer (FRET) melting experiments. CD titrations revealed a

stabilization higher than 30 °C in the case of c-MYC G4 structure and, for the same sequence, DPP(PyMe)$_2$ showed the ability to block the activity of *Taq* polymerase in a dose-dependent manner. The subcellular localization obtained with confocal microscopy corroborates the results obtained by the other techniques and the obtained data suggests that DPP(PyMe)$_2$ is an attractive ligand for the development of G4 labelling probes.

Keywords

G-quadruplexes, telomeric G4, oncogene promoters, G4 ligands, mixed binding mode, loop/groove

1.   Introduction

During cell division, telomeres undergo shortening as a result of interruptions in the DNA replication process. As a defense, the reverse transcriptase enzyme telomerase adds specific and repetitive DNA sequences to the 3' telomere end of the chromosomes, preventing the mechanism involved in telomeres shortening.[1] The over-expression of this enzyme was identified in almost 90% of human cancers[2] and telomerase has been recognized as a target for the development of new anticancer drugs. Other important targets for anticancer agents are tumour suppressor genes and oncogenes (a mutated version of proto-oncogenes responsible by encoding proteins for normal cell division, stimulation and death end) due to their closely association with the initiation and progression of tumours.

The possibility of targeting secondary structures, such as the G-quadruplexes (G4) present in most human oncogene promoters, and also in telomeres, using interactive ligands is being considered a promising antineoplastic strategy since can contribute to downregulate transcription or to

block telomere elongation in cancer cells, by stalling the DNA replication machinery.[3]

More specifically, the presence of G4 at the end of telomeres (whose function is to protect their ends from nuclease attack) enables indirect targeting of telomerase.[4-6] G4 are recognized and partially unwound by telomerase for 3' end extension, thus binding of stabilizing compounds to G4 structures will "lock" the telomeres in the quadruplex configuration, preventing telomere lengthening by telomerase (Figure 1).[7]
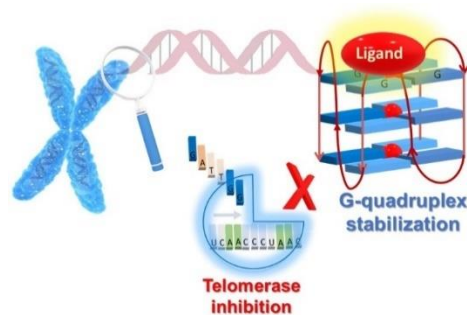

Figure 1 - Indirect telomerase inhibition by G-quadruplex stabilization by ligands.

G4 structures are also present in other genome regions such the 5' and 3' untranslated regions (UTRs), recombination hotspots, transposable elements (TEs), among others.[8-14] Due to G4 conformation diversity and to the correlation between G4 structure, stabilizing ligands and resolution by helicase, quadruplex structures are considered to be strongly controlled during specific cellular processes and are being recognized to have an important regulatory role in genes transcription, translation, replication initiation, recombination, aptamer binding and mRNA processing.[10,15-20] More recently, it has been shown that the presence of G4 structures is also tightly associated with cytosine-guanine (CpG) dinucleotide islands hypomethylation in the human genome; this DNA methylation level is a critical factor for gene regulation.[21]

So, considering that the stabilization of G-quadruplexes can open new perspectives in terms of anticancer therapeutics, the efficacy of some molecules

3

to stabilize G4 strucures with the consequent telomerase inhibition and regulation of gene expression has been evaluated using different biophysical and biochemical methods with promising results.[22-31]

It is accepted that the G4 recognition can occur through outside stacking on the ends of the G-tetrad core, also known as end-stacking, interaction with the backbone (core and *loop* bases) known as *groove* or *loop* binding and by intercalation.[32] Since the G4 structure is rigid and stable, the distortion caused by a hypothetic intercalation of a ligand will have a higher energetic cost than the outside stacking on the top, *loops* or *grooves*, seen as the more favourable binding modes.[33] Thus, to our knowledge, ligand intercalation in G4 structures was never experimentally demonstrated.

Structural attributes of ligands such as the presence of a heteroaromatic moiety that can interact on the G-quartet surface of a quadruplex by $\pi-\pi$ stacking and flexible cationic charged terminal side chains are pointed as essential features for effective ligand binding to a quadruplex structure.[4] Other important structural characteristics are the presence of bulky substituents, to prevent intercalation with double-stranded DNA, and high affinity for G4s ($K_b \geq 10^6$ M^{-1}). The solubility of DNA ligands in aqueous media is also an essential aspect.

Some of these structural features are present in ligands such as those depicted in Figure 2, that have recognized activity as G4 stabilizers and telomerase inhibitors. Among them, the fused heteroaromatic polycyclic derivative Quarfloxin is the only G4 interactive small molecule reaching phase II clinical trials.[4] The two macrocycles Telomestatin and the cationic 5,10,15,20-tetrakis(*N*-methyl-4-pyridinium)porphyrin (TMPyP), are one of the most active known G4 ligands[34] and one of the most studied tetrapyrrolic derivative,[28,35] respectively. Other ligands, with non-fused heteroaromatic structures, like Pyridostatin and analogues are also known to present striking growth-inhibitory effects on cancer cell lines after a few days of exposure.[36]

Metalloorganic complexes such as salphen and terpyridine derivatives, are also meriting the attention of the scientific community.[35]
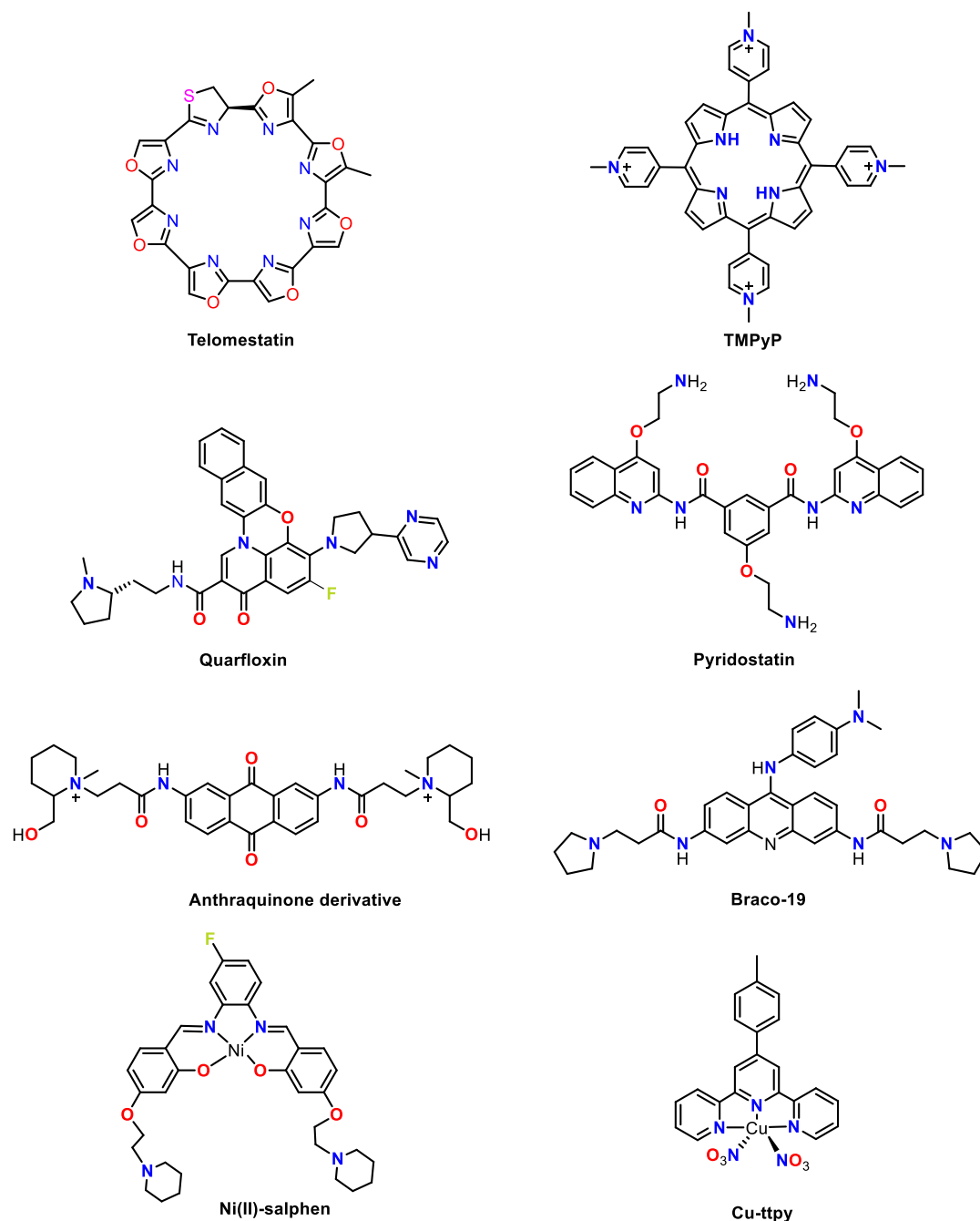

Figure 2 – Examples of ligands that are G4 stabilizers.

Substituted anthraquinones[37] and tri-substituted acridines, such as BRACO[38] (Figure 2), owning a planar backbone, intrinsic fluorescence and cellular uptake with known nucleus penetrating ability, are described to interact with G4 by quartet stacking or in quadruplex *grooves* and *loops*.[39-42]

Diketopyrrolopyrroles (DPP) are a family of small molecules with a planar structure that can induce strong $\pi-\pi$ stacking with neighboring molecules and intermolecular hydrogen bonding. These heterocycles represent a class of brilliant red and strong fluorescent high-performance dyes and pigments, that gained wide attention in recent years due to their outstanding properties. The excellent photostability, high fluorescent quantum yields, and environment and thermal stability makes them excellent candidates as fluorescent sensors. The potential biological application of DPP, namely in photodynamic therapy, has been reported in recent years.[43-47] Additionally, due to their chemical stability and solubility in aqueous media, these molecules were also described as good fluorescent DNA biosensors.[48,49]

Following our interest in developing molecules with adequate features to act as G4 ligands,[28,31,50-52] a new dicationic DPP derivative (DPP(PyMe)$_2$, (Figure 3 and Scheme 1) was designed, synthetized and investigated as a potential ligand for G4. To our knowledge, this is the first example of using the DPP scaffold in the design of G4 ligands, opening new perspectives in terms of G4 labelling agents.

The interactions of this new molecule with G4 structures (see Table 1), formed in telomeric [AG$_3$(T$_2$AG$_3$)$_3$] and in oncogene (c-MYC, KRAS-22-RT) promoter regions, and with double stranded DNA structures (ds26 and *calf thymus*) were evaluated. The presence of positive charges in DPP(PyMe)$_2$ structure increased its solubility in the water while also enhancing its electrostatic interactions with the negatively charged DNA structures.
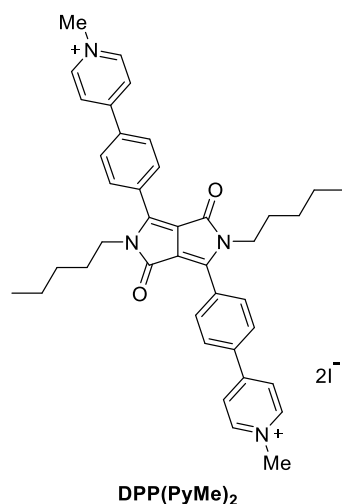
Figure 3 - Structure of the DPP(PyMe)$_2$

The stability of DPP(PyMe)$_2$–DNA quadruplex and duplex conformations was evaluated using UV-Vis titrations. The analysis of the hypochromic and bathochromic effects in the ligand UV-Vis spectra suggested a high affinity of this molecule for G4 conformations.

Several complementary methods, namely fluorescence, circular dichroism (CD), polymerase chain reaction (PCR) and confocal microscopy, were used in these studies to confirm the ligand affinity, to evaluate its selectivity towards G4, ability to block the activity of *Taq* polymerase and cellular localization.

2. Materials and methods

2.1. *Chemicals*

The chemicals were purchased as analytical grade and used without further purification. Lyophilized DNA oligonucleotides were purchased from Eurogentec (Belgium). When required, aqueous solutions were prepared in MiliQ water.

For oligonucleotides the provided molar extinction coefficient values were considered. Stock solutions of DPP(PyMe)$_2$ were prepared in DMSO and stored

at 4 ºC. Before each assay, an aliquot of the stock solution was diluted to the desired final concentration in PBS buffer.

The solvents were used as received or distilled and dried by standard procedures.[53] Analytical thin layer chromatography (TLC) was carried out on precoated sheets with silica gel (Merck 60, 0.2 mm thick). Column chromatography was carried out using silica gel (Merck, 35–70 mesh). ^{1}H and ^{13}C NMR spectra were recorded on Bruker Avance 300 or Bruker Avance 500. CDCl$_3$ and DMSO-d_6 were used as the deuterated solvents and tetramethylsilane (TMS) as the internal reference. The chemical shifts are expressed in δ (ppm) and the coupling constants (J) in Hertz.

2.2. Preparation of DNA structures (double-stranded and G-quadruplexes)

A PBS solution containing 20 mM of phosphate buffer (10 mL of KH$_2$PO$_4$ 1 M and 200 μL of K$_2$HPO$_4$ 1 M) and 100 mM of KCl was prepared with pH adjusted to 6.8. The PBS solution was used as the solvent for oligonucleotide solutions.

After solubilisation in PBS, each oligonucleotide was heated up to 85 °C for 10 min and left to cool overnight to assure the correct folding into double-stranded or G4 structures. The solutions were stored at -20 °C. The sequences and abbreviation of the studied G4 and double-strandedDNA structures are presented in **Table 1**.

Table 1. Sequence, occurrence and abbreviation of studied oligonucleotides

Oligonucleotide sequence	Occurrence	Abbreviation
5'-A**GG** GTT A**GG** GTTA**GG** GTT A**GGG**-3' (human telomeric repeat)	Telomere	AG$_3$(T$_2$AG$_3$)$_3$
5′- TGA **GGG** T**GG** GTA **GGG** T**GG** GTA A-3'	Oncogene promoter	c-MYC
5′ – A**GG** G**CG** G**TG** T**GG** GAA TA**G GGA** A-3'	Oncogene promoter	KRAS-22-RT
5′-AGGGCGGTGTGGGAAGAGGGAAGAGGGGGAGG-3′	Oncogene promoter	KRAS-32R
5′-CAA TCG GAT CGA ATT CGA TCC GAT TG-3′	Double-stranded DNA	ds26

Long double strand DNA	Double-stranded DNA	CT

2.3 – Synthesis of the dicationic diketopyrrolo[3,4-c]pyrrole DPP(PyMe)$_2$

2.3.1 – Synthesis of the neutral pyridyl precursor **DPPPy$_2$**

To a suspension of DPPCl$_2$ (0.100 g, 0.201 mmol), 4-pyridylboronic acid (0.320 g, 2.01 mmol) and K$_3$PO$_4$ (0.270 g, 0.804 mmol) in butan-1-ol (20.0 mL) were added a catalytic amounts of Pd(OAc)$_2$ (5%) and SPhos (10%). The resulting mixture was heated at reflux overnight under a nitrogen atmosphere and then it was left to cool down to room temperature. The mixture was diluted with CH$_2$Cl$_2$ and water, the organic layer was separated and washed with water and brine. The product was purified by preparative TLC using a mixture of dicloromethane/hexane (2:1) as eluent. Compound DPPPy$_2$ was obtained in 51% yield. Mp: 251.8–252.4 °C; ^{1}H NMR (CDCl$_3$, 300 MHz), δ (ppm): 8.74 (4H, d, J = 6.0 Hz), 7.99 (4H, d, J = 9.0 Hz), 7.84 (4H, d, J = 9.0 Hz), 7.62 (4H, d, J = 6.0 Hz), 3.81 (4H, t, 7.5 Hz), 1.69–1.73 (4H, m), 1.24–1.29 (8H, m), 0.85 (6H, t, J = 6.0 Hz). ^{13}C NMR (CDCl$_3$, 75 MHz), δ (ppm): 162.7, 150.4, 147.8, 147.2, 140.7, 129.5, 128.8, 121.6, 110.3, 42.1, 29.3, 28.9, 22.2, 13.9. MS (ESI) m/z: 583.5 [M+H]$^+$, 292.5 [M+2H]$^{2+}$. HRMS-ESI(+): m/z calcd for C$_{37}$H$_{43}$O$_6$ 583.3054 [M+H]$^+$, found 583.3056.

2.3.2 – Methylation of DPPPy$_2$

To a solution of DPPPy$_2$ (30 mg) in DMF (3 mL) in a sealed tube was added methyl iodide (16 µl, 4 equiv.). The mixture was stirred for at room temperature until total conversion of the starting material (5 h). Diethyl ether (10 ml) was added to the solution to form a suspension, wich was filtered and rinsed with additional diethyl ether. The compound was dried and obtained in quantitive yield (30.6 mg). Mp: 272.8–274.4 °C; ^{1}H NMR (DMSO, 300 MHz), δ (ppm): 9.09 (4H, d, J = 6.0 Hz), 8.63 (4H, d, J = 6.0 Hz), 8.33 (4H, d, J = 9.0 Hz),

8.12 (4H, d, J = 9.0 Hz), 4.37 (6H, s), 3.79 (4H, t, J = 7.5 Hz), 1.43–1.48 (4H, m), 1.13–1.23 (8H, m), 0.76 (6H, t, J = 6.0 Hz). ^{13}C NMR (DMSO, 75 MHz), δ (ppm): 161.9, 153.3, 147.6, 146.3, 136.3, 131.1, 130.2, 129.1, 124.9, 110.3, 47.7, 41.4, 28.8, 28.62, 21.9, 14.2; HRMS-ESI(+): m/z calcd for $C_{40}H_{44}O_2N_4$ 306.1727 M^{2+}, found 306.1724.

2.4. UV-Vis spectroscopy

UV-Vis absorption spectra were recorded in a Shimadzu UV-2501-PC spectrophotometer in the range between 350-700 nm, using a quartz cuvette of 1 cm length; the temperature was controlled at 25 ºC using a Huber Compatible Control CC1. The titrations were performed by successive additions of the adequate oligonucleotide solution to a solution of DPP(PyMe)$_2$ in PBS with the initial concentration of 5 μM and were ended after 3-5 values of constant absorbance.[54] The dilution effects in the spectra were mathematically corrected using the formula Abs_{cor} = [(Vi+Vad)/Vi]*Abs, where Abs_{cor} is the corrected absorbance, Vi is the initial volume of the ligand in the cuvette, Vad is the volume of DNA added and Abs is the absorbance of each point of the titration. To ensure the reproducibility of results, all experiments were performed in triplicate.

The percentage of hypochromicity of the absorption band was calculated using the following equation: % hypochromicity = [($Ɛ_{free}$ - $Ɛ_{bound}$)/$Ɛ_{free}$]×100, where $Ɛ_{bound}$ was calculated using the Beer's Law ($Ɛ_{bound}$ = A_{bound}/C_{bound}) and $Ɛ_{free}$ is the extinction coefficient value calculated, in PBS, for DPP(PyMe)$_2$, $Ɛ_{487}$ = 19152 M^{-1}cm^{-1}.

Method of continuous variation, or Job plot method, was used in order to obtain the binding stoichiometries. Job diagrams were obtained by plotting F(χ) against the molar fraction of the ligand (χ), according to the expression:

$$F(\chi) = \frac{A_{obs} - (C_{lig}.Ɛ_{lig} + C_{DNA}.Ɛ_{DNA})}{C_{lig} + C_{DNA}} \qquad (2)$$

where A_{obs} corresponds to the observed absorbance of the solution after each DNA addition, C_{lig} and C_{DNA} correspond, respectively, to the total concentration of DPP(PyMe)$_2$ and DNA, and ε_{lig} and ε_{DNA} are the extinction coefficients of the DPP(PyMe)$_2$ and DNA structure, respectively, at a given wavelength. The stoichiometry corresponds to the maximum or minimum observed.

2.4. Fluorescence

2.4.1 - Fluorescence Titrations

The spectra obtained from fluorescence titrations were recorded in a Horiba FluoroMax-4 spectrofluorometer at 25 °C and using a quartz cuvette with a path length of 1 cm. As before, the ligand was excited at 485 nm and the fluorescence emission collected between 500-750 nm; the excitation and emission slits were fixed at 5 nm. The association constant between each G4 and the ligand was assessed by measuring the change in fluorescence after titrating the ligand solution at 2.5 μM with the adequate oligonucleotide at concentrations varying between 0 to 4.7 μM. Data was converted into fraction of bound ligand (α) plots using the following equation:

$$\alpha = \frac{I - I_\lambda^{free}}{I_\lambda^{bound} - I_\lambda^{free}}$$

where I is the fluorescence intensity of each ligand:G4 ratio and I_{free} and I_{bound} are the fluorescence intensity of the free and fully bound ligand, respectively. Data points were then fitted (see Figure S1) to a hyperbolic function (OriginPro 8) and K_D values were determined from the following saturation binding model:

$$\alpha = \frac{[DNA]^h}{K_D + [DNA]^h}$$

where α is the fraction of ligand bound, [DNA] is the concentration of the DNA and n is the Hill constant which describes cooperativity of ligand binding.

2.4.2 – Fluorescence Intercalator Displacement (FID) studies

For the fluorescence displacement studies, stock solutions of each oligonucleotide at 10 μM and of thiazole orange (TO) at 35 μM were prepared. The previous solutions were mixed, in the proportion of 1:1, and after 10 min of orbital shaking at 500 rpm, the fluorescence of the obtained TO-oligonucleotide complex was measured in a Fluoromax-3 spectrofluorometer (Horiba), using the excitation wavelength at 485 nm and analyzing the emission between 510-750 nm; the excitation and emission slits were set at 10 nm.

The DPP(PyMe)$_2$ ligand was then added to each TO-oligonucleotide solution at concentrations ranging from 0 to 4 μM. The resulting fluorescence was measured using the previous experimental parameters. The percentage of displacement was calculated using the equation:

$$\% \, displacement = 100 - \frac{F_A}{F_{A0}} * 100$$

where $F_A = F - F_{H2O}$ and $F_{A0} = F_0 - F_{H2O}$; F is the fluorescence intensity of each sample, F_{H2O} the fluorescence intensity of mili-Q and F_0 the fluorescence from the fluorescent probe bound to DNA without added ligand. The DC_{50} corresponds to the concentration for which 50% of TO was displaced from the DNA structure.

2.4.3 - Fluorescence Resonance Energy Transfer (FRET) melting studies

FRET-melting experiments were performed in a 96-well plate using a CFX Connect™ Real-Time PCR Detection System (Bio-Rad, USA), equipped with a FAM filter (λ_{ex} = 492 nm; λ_{em} = 516 nm). The c-MYC and KRAS 32R oligonucleotides were labelled with fluorescein (FAM) and tetramethylrhodamine (TAMRA). In order to assess the selectivity of the ligand to the G4 sequences, FdxT d(TATAGCTAT-hexaethyleneglycol-TATAGCTATA) also labelled with FAM and TAMRA was used. The measurements were performed in 10 mM lithium cacodylate (pH 7.2)

supplemented with 10 mM KCl + 90 mM LiCl for c-MYC and KRAS 32R, and 100 mM KCl for FdxT. The experiments were performed with the oligonucleotides at 0.2 μM and the ligand concentration used were 0.2, 0.4, 0.8, 1.6 and 3.2 μM. The oligonucleotide solutions were annealed at 95 °C by 10 min, following by a slowly cooling in ice for 30 min. For competition studies, 3 and 10 μM of double-stranded ds26 was added to the wells. Subsequently, samples were incubated 30 min at room temperature. After an initial incubation at 25 °C for 5 min, the thermocycler was set to perform a stepwise increase of 1 °C every 1 min, from 25 °C to 95 °C, and the FAM emission measures after each step. The melting temperatures were determined from the normalized curves as the temperature for which the normalized emission was 0.5. Selectivity Factor (S factor) corresponds to the relative DPP(PyMe)$_2$ stabilization remaining in the presence of the competitor[55] and was determined using the following equation.

$$S \, factor \; = \frac{\Delta T_m \, in \, presence \, of \, competitor}{\Delta T_m \, without \, competitor}$$

2.5 - Time dependent Density-functional theory (TD-DFT) calculations

All calculations were carried out using the Gaussian16[56] software package without symmetry constrains. Density Functional Theory (DFT)[57] and Time-Dependent DFT (TD-DFT)[58] were used for computation of the ground state and vertical excitations, considering the 12 lower lying transitions. See SI for details.

2.6 - Circular dichroism (CD) spectroscopy

CD spectra were acquired in a Jasco J-815 spectrometer (Jasco, USA), using a Peltier temperature controller (model CDF-426S/15). G4 oligonucleotides were annealed as previously described. The experiments were performed in a quartz cell with an optical length of 1 mm at 25 °C. CD spectra were recorded using an instrument scanning speed of 200 nm min^{-1} with a response time of 1 s through wavelengths ranging from 220 to 340 nm. The

recording bandwidth was 1 nm with 1 nm step size. For CD titration, 10 μM strand concentration of oligonucleotides was used in 20 mM phosphate buffer (10 mM KH_2PO_4, 10 mM K_2HPO_4, pH 7.1) containing 1 mM KCl + 99 mM LiCl for c-MYC, and 10 mM KCl + 90 mM LiCl for KRAS 22RT, KRAS 32R and telomeric sequences.

A stock solution of 10 mM of the ligand was prepared in DMSO. The volume required for the titrations was added to the quartz cell.

CD melting studies were performed in the temperature range 25–95 °C with a heating rate of 2 °C min^{-1} by monitoring the ellipticity at 262 nm. Spectra were acquired in the range of 0 to 8 molar equivalents of ligand.

$$f = \frac{CD - CD_\lambda^{min}}{CD_\lambda^{max} - CD_\lambda^{min}}$$

Data were converted into fraction folded (θ) plots using the aforementioned equation and fitted to a Boltzmann distribution (OriginPro 2016) and the melting temperature (T_m) was obtained.

2.7 - PCR-stop assay

PCR stop assay experiment was performed to evaluate the binding and stability of c-MYC G4 structure by DPP(PyMe)$_2$ ligand. The oligonucleotides used in this study were Pu77 (intramolecular c-MYC G4 structure), Pu77-mut and primer RevPu77, and are presented in **Table 2**. Oligonucleotides at a final concentration of 10 μM were annealed in 20 mM phosphate buffer (10 mM KH_2PO_4, 10 mM K_2HPO_4, pH 7.1) and 100 mM KCl by heating to 90 °C during 10 min, and gradually cooled to room temperature. Each reaction mixture was performed to a final volume of 25 μL containing the annealing buffer, 0.2 mM dNTPS, 400 nM of each DNA template and 100 nM primer. The reactions were further incubated with different concentrations of the ligand (0.8 μM, 1.6 μM, 3.2 μM, 6.4 μM and 12.4 μM) for 1 h at room temperature. Thereafter, 1 unit of *Taq* DNA polymerase was added, and the reaction mixture was incubated in a

thermal cycler (Bio-Rad, Hercules, USA) with the following cycling conditions: 94 °C for 2 min, followed by 30 cycles of 94 °C for 30 s, 58 °C for 30 s and 72 °C for 30 s. PCR products were resolved on a 15% non-denaturing polyacrylamide gel in TBE 1× and stained with stains-all solution under continuous and gentle agitation overnight followed by discoloration in water before visualization.

Table 2. List of the oligonucleotides used in the PCR-stop assay.

Oligonucleotide	Sequence (from 5′ to 3′)	Description
Pu77myc	TCCAACTATGTATACTGGGGAGGGTGGG GAGGGTGGGGAAGGTTAGCGGCACGCA ATTGCTATAGTGAGTCGTATTA	Wild-type *c-myc* template
Pu77-mut	TCCAACTATGTATACT**AAGGAAAGTAA GGAAAGTAAGG**AAGGTTAGCGGCACG CAATTGCTATAGTGAGTCGTATTA	Mutant *c-myc* template
RevPu77 complementary sequence	TAATACGACTCACTATAGCAATTGCGTG	Primer

2.8 – In silico studies

Molecular docking studies were performed with four different high-resolution DNA G4 structures (telomeric G4 (PDB: 4G0F), c-MYC (PDB: 1XAV), KRAS 22R (PDB: 5I2V) and KRAS 32R (PDB: 6SUU)) and the ligand DPP(PyMe)$_2$ using AutoDockTools package. Both the G4 structure and ligand was first optimized for docking using the DockPrep tool of USCF Chimera software. After assigning empirical atomic partial charges (Gasteiger) and polar hydrogens, docking simulations were carried with AutoDock 4.2.6 program using Lamarckian genetic algorithm. The grid was placed on the entire G4 structure. Each run consisted of an initial population of 150 random individuals, a maximum number of evaluations set to 2.5×10^7, the rate of mutation and crossover set to 0.02 and 0.8, respectively, and an elitism value of 1. All torsions of the ligands were set as flexible while the structure of the G4

was kept rigid. Each run provided 10 different ligand structures. The most representative structures were selected based on the binding free energy.

The most energetically favourable binding poses were energy minimized using GROMACS 2020.6 package. Ligand topology was generated using ACPYPE server[59]. Energy minimization was carried out using AMBER DNA OL15 force field[60] and TIP3P water model. DNA-ligand complexes were solvated in a 10 Å dodecahedron box. K^+ counterions were added to neutralize the system total charge. Energy minimization (steepest descent algorithm) was run for a maximum of 50000 steps until the maximum force < 10.0 kJ/mol. Unless otherwise stated, each replicate was then simulated for 100 ns, using the particle mesh Ewald (PME) method to treat long-range electrostatic interactions with a Fourier grid spacing of 0.16 nm and a cut-off of 1.2 nm for direct contributions. Lennard–Jones interactions were calculated using a neighbour pair list with a cut-off of 1.2 nm and using a Verlet scheme[61] . The temperature was maintained at 300 K using a modified Berendsen thermostat and the pressure was kept constant by Parrinello-Rahman barostat. Coordinates were collected in trajectory files every 10 ps. MD trajectories were analysed with VMD 1.9.3 and representative images were rendered using UCSF ChimeraX 1.2.5 software. 2D diagrams of G4/DPP(PyMe)$_2$ complexes were determined by using LigPlot+ v.2.2.4.

2.10 - Confocal microscopy

Normal human dermal fibroblasts (NHDF) were grown in RPMI medium, supplemented with 10% FBS, 1% streptomycin-penicillin antibiotic, 0.01 M HEPES, 0.02 M L-glutamine and 1 mM sodium pyruvate. Additionally, the HeLa cervical cancer cell line was grown in DMEM medium, supplemented with 10% FBS and 1% streptomycin-penicillin antibiotic. Cultures were maintained in a humidified chamber at 37 °C and 5% CO_2. The cell lines were subsequently harvested, counted using the trypan blue exclusion method and

seeded in µ-slide 8-well flat bottom imaging plates (Ibidi GmbH, Germany) at a plating density of 1×10^5 cells/mL and incubated for cell attachment for 24 h at 37 °C and 5% CO_2. Thereafter, cells were washed 3 times with PBS $1\times$ and stained with Hoechst 33342® nuclear probe (1 µM) for 15 min. Subsequently, the cells were washed 3 times with PBS $1\times$ to remove the excess of probe and incubated with DPP(PyMe)$_2$ (10 µM). Thereafter, the cells were transferred to a Zeiss LSM 710 confocal laser scanning microscope (CLSM; Carl Zeiss SMT Inc., USA) equipped with a plane-apochromat 63×/DIC objective and processed in Zeiss Zen software, in order to evaluate the cellular colocalization and uptake. The fluorescence images were obtained at 40× magnification.

3 - Results and Discussion

3.1 - Synthesis and structural characterization of the dicationic diketopyrrolo[3,4-c]pyrrole derivative DPP(PyMe)$_2$

The new dicationic diketopyrrolo[3,4-c]pyrrole DPP(PyMe)$_2$ was prepared in three steps, as illustrated in scheme 1, starting from the commercially available dichlorinated DPP derivative Pigment Red 254. After the N,N-dialkylation with 1-iodopentane as previously reported,[62] the neutral pyridyl precursor DPPPy$_2$ was obtained in 51% yield by a Suzuki-Miyaura reaction between DPPCl$_2$ and 4-pyridylboronic acid, following a recently reported procedure.[63] The quaternization of the pyridyl groups with methyl iodide afforded the desired dicationic derivative DPP(PyMe)$_2$ in quantitative yield.
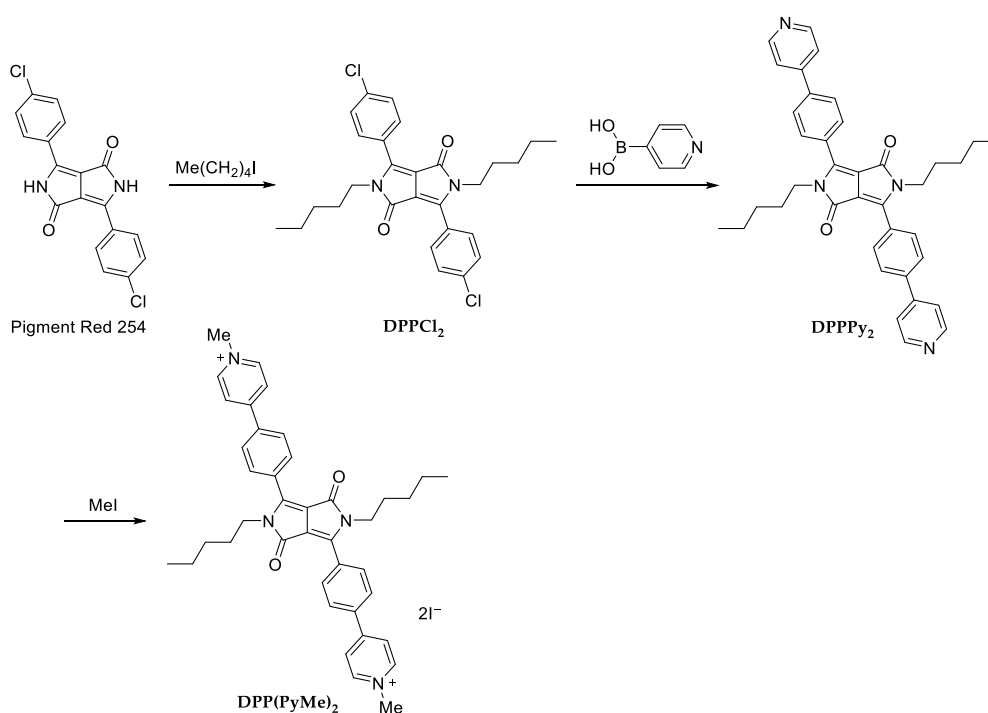
Scheme 1 - Synthetic route to the dicationic DPP derivative.

The structures of the neutral scaffold and of the dicationic ligand were unambiguously established from their NMR and mass spectra (see experimental part and also SI, figures S1-S7). The ^{1}H NMR spectrum of the

dicationic DPP(PyMe)$_2$ when compared with the neutral precursor DPPPy$_2$, displays, as expected, an extra singlet at 4.37 ppm due to the resonance of the six *N*-CH$_3$ protons.

The molecular weight of both derivatives was confirmed by mass spectrometry (MS-ESI and HRMS-ESI); the spectrum of the neutral derivative showed the presence of two peaks at *m/z* 583.5 and 292.5, corresponding respectively to [M+H]$^+$ and [M+2H]$^{2+}$. The spectrum of the dicationic derivative showed a peak at 306.2 corresponding to the M^{2+} ion.

The absorption and emission spectra of DPP(PyMe)$_2$ are shown in Figure 4. The absorption spectrum displays two bands at 322 nm and 488 nm and the emission spectrum revealed a Stokes shift of 99 nm when the sample was excited at 488 nm. The fluorescent quantum yield or Ø$_F$ of DPP(PyMe)$_2$, in dimethylformamide (DMF) is 0.77.
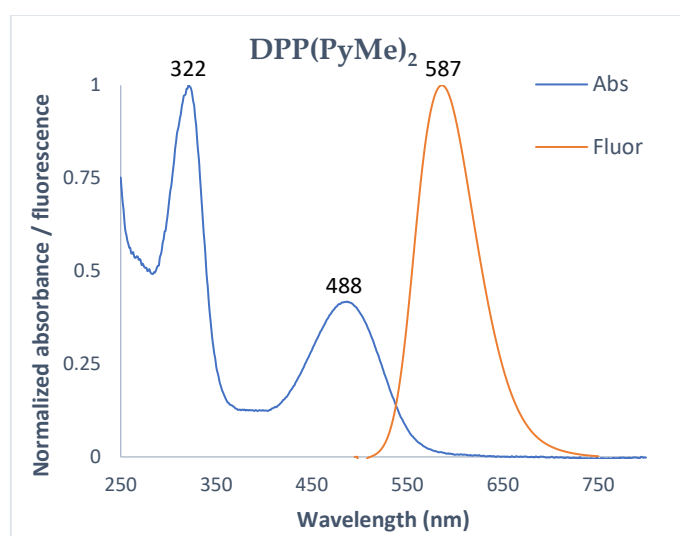

Figure 4 – Normalized absorbance and fluorescence spectra of DPP(PyMe)$_2$ (λ_{exc} = 488 nm) obtained in PBS solutions (5 and 2.5 uM, respectively)

The development of photostable fluorescent dyes with large Stokes shifts (> 80 nm) is particularly relevant for biological applications.[64,65] These
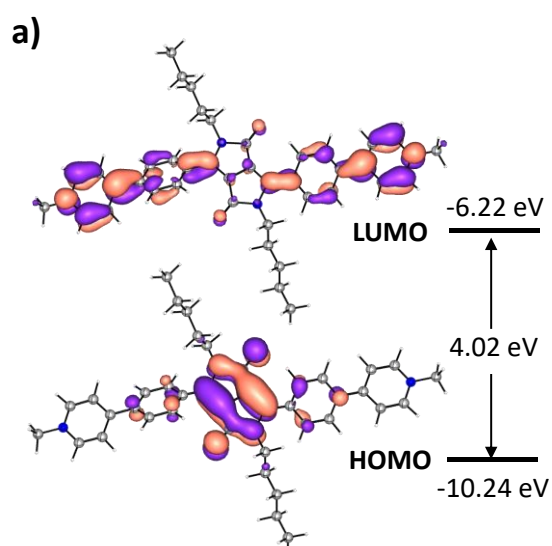
large Stokes shift can minimize the cross-talk between the excitation source and the fluorescent emission improving the signal-to-noise ratio for cellular imaging. Besides, the photostability of this type of dyes is also beneficial when noninvasive long-term cellular imaging is being investigated.[65] The molecular relaxation following DPP-PyMe excitation was studied by time-dependent density functional theory calculations (TD-DFT) in order to shed light on the electronics of the system and the reason behind the large Stokes shift.

3.2 - Time-dependent density functional theory calculations (TD-DFT)

The vertical excitations of the molecule were studied by TD-DFT at the CAM-B3LYP/6-31G(d,p)[66] level of theory after optimization in gas phase (see Table S1 for detail in the first six transitions). The preliminary analysis of the frontier orbitals shows that the HOMO of the system is located at the diketopyrrolopyrrole unit while the LUMO is mostly spread among the peripheral aromatic moieties (Figure 5a). The least energetic transition ($S_0 \rightarrow S_1$) calculated is only 0.17 eV underestimated by the method (λ_{exp} = 488 nm vs λ_{cal} = 522 nm). This is in good agreement with the experimental data and the discrepancy attributed to solvatochromic effects not considered in the gas-phase calculations. Analysis of other vertical excitations shows that the next transition in the absorbance spectrum should correspond to $S_0 \rightarrow S_4$ as small oscillator strength values (f<0.01) were determined for lower excited states, despite the underestimation by the method (0.29 eV, λ_{exp} = 322 nm vs λ_{cal} = 348 nm).

The least energetic transition is clearly dominated by the HOMO $\rightarrow$ LUMO transition (lower inset table in Figure 5b), being accompanied by a small contribution of excitation to LUMO+2. As the vertical transition is mostly composed by excitation between the frontier orbitals, this translated into the dominance of an intramolecular charge transfer from the heterobicyclic

core of the molecule into the peripheral aryl substituents. The graphical analysis of the natural transition orbitals (Figure 5b), shows that the charge transfer is accompanied by considerable local excitation at the central fused rings, accompanied by excitation at the phenyl rings, while the pyridyl rings work solely as electron-acceptor units. The band at 322 nm, assigned to the $S_0 \rightarrow S_4$ transition is mostly derived from electron occupation of the LUMO+2 orbital, from HOMO. This corresponds to local excitation of the diketopyrrolopyrrole core accompanied with partial charge transfer to the peripheral pyridyl substituents.
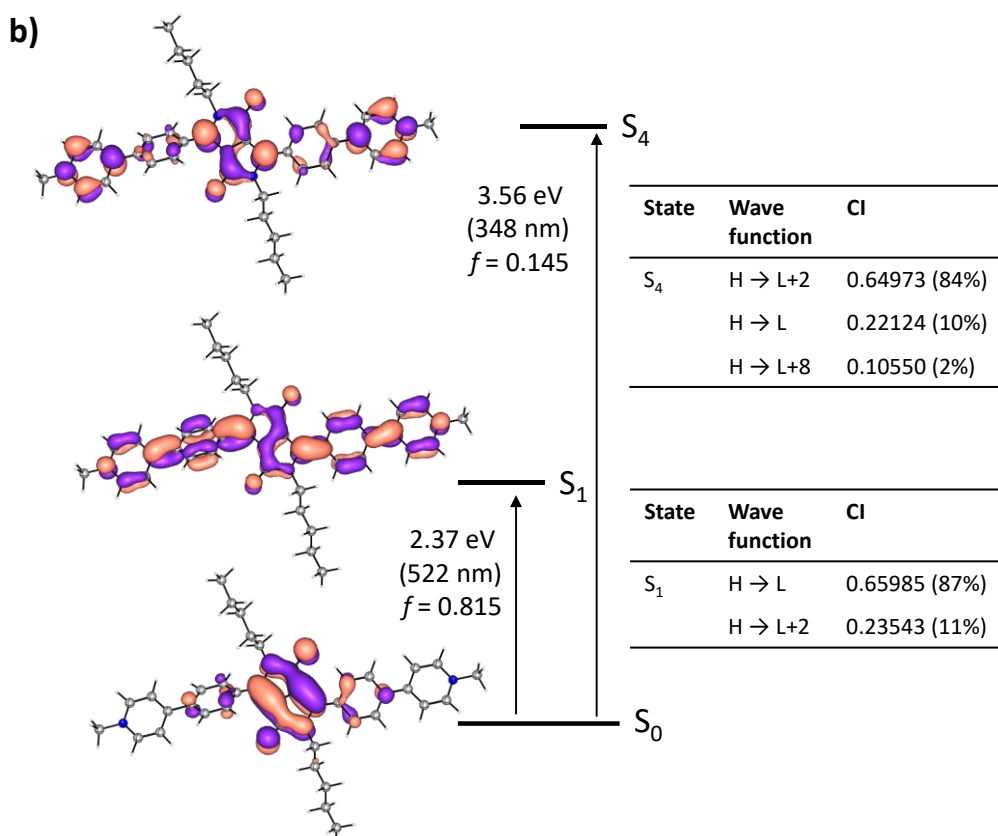
a)

b)

State	Wave function	CI
S_4	H → L+2	0.64973 (84%)
	H → L	0.22124 (10%)
	H → L+8	0.10550 (2%)

3.56 eV
(348 nm)
f = 0.145

S_4

S_1

2.37 eV
(522 nm)
f = 0.815

S_0

State	Wave function	CI
S_1	H → L	0.65985 (87%)
	H → L+2	0.23543 (11%)

Figure 5 - a) Graphic representation of frontier molecular orbitals and respective energies; b) Graphic representation of natural transition orbitals and wave functions involved in the 1st and 4th vertical excitations, obtained at TDDFT/CAM-B3LYP/6-31G(d,p) based on optimized ground state geometries in gas phase.

In order to characterize the impact of the excitation on the conformation of the molecule, the geometry of the lowest excited state S_1 was optimized at TD-DFT to find the minimum energy point in the excited state potential energy surface. The comparison of the ground state geometry and the resultant geometry upon excitation (Figure 6) shows a planarization of the aromatic system. The angles between the π-system of the peripheral aromatic rings with the central diketopyrrolopyrrole change from average 30.27° to 20.97°, accompanied by the pyridyl substituents and the phenyl ring

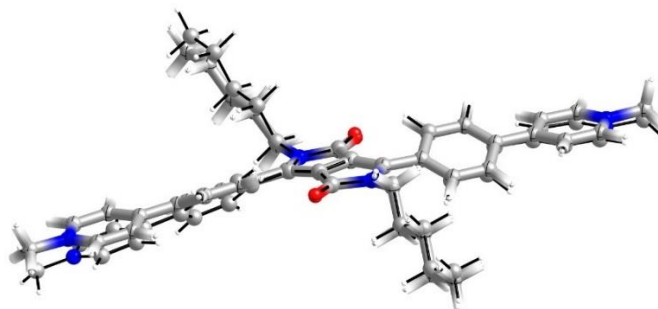approaching to coplanarity by decreasing the angles from -31.71° to -22.76° (average values).

Figure 6 - Overlap of optimized geometries of S_0 (balls and sticks) and relaxed S_1 (sticks) at CAM-B3LYP/6-31G(d,p) level of theory.

3.3 - UV-Vis Spectroscopy

The electronic absorption spectrum of DPP(PyMe)$_2$ prompted us to monitor its interactions with the selected oligonucleotides AG$_3$(T$_2$AG$_3$)$_3$, c-MYC, KRAS-22-RT, ds26 and CT (see Table 1) using UV-Vis spectroscopy. In general, the alterations observed on the position and intensity of the ligand absorption band maximum (batho or hypsochromic shifts and hypo or hyperchromic effects) at the end of the titrations can give an important insight about the affinity, selectivity and type of interaction of the binding process.

When *groove* or outside bindings are involved, since less direct contact between π-systems occurs, less pronounced changes in the UV-Vis absorption spectra are expected and red shifts lesser than 8 nm have been described.[67,68] Typical values of hypochromicity (higher than 35%) and red shifts ($\Delta\lambda$) higher than 15 nm in the UV-Vis bands are expected when intercalative binding processes take place. Precaution must be taken regarding these values as reference since they were determined for long pieces of duplex DNA where the end-stacking is not significant.[69]

The alterations observed in the DPP(PyMe)$_2$ UV-Vis absorption spectrum during the successive additions of each DNA sequence in a phosphate buffer

(PBS) are summarized in Figure 7 (see also Table 3). These titrations were performed with DPP(PyMe)₂ at an initial concentration of 5 µM and were stopped after the addition of 195 µl of the oligonucleotide. This amount was considered since no significative changes were observed for both double-stranded sequences (*calf thymus* and ds26) after three consecutive additions. We decided to consider this point for ending also the titrations with the G4 sequences for comparative purposes.
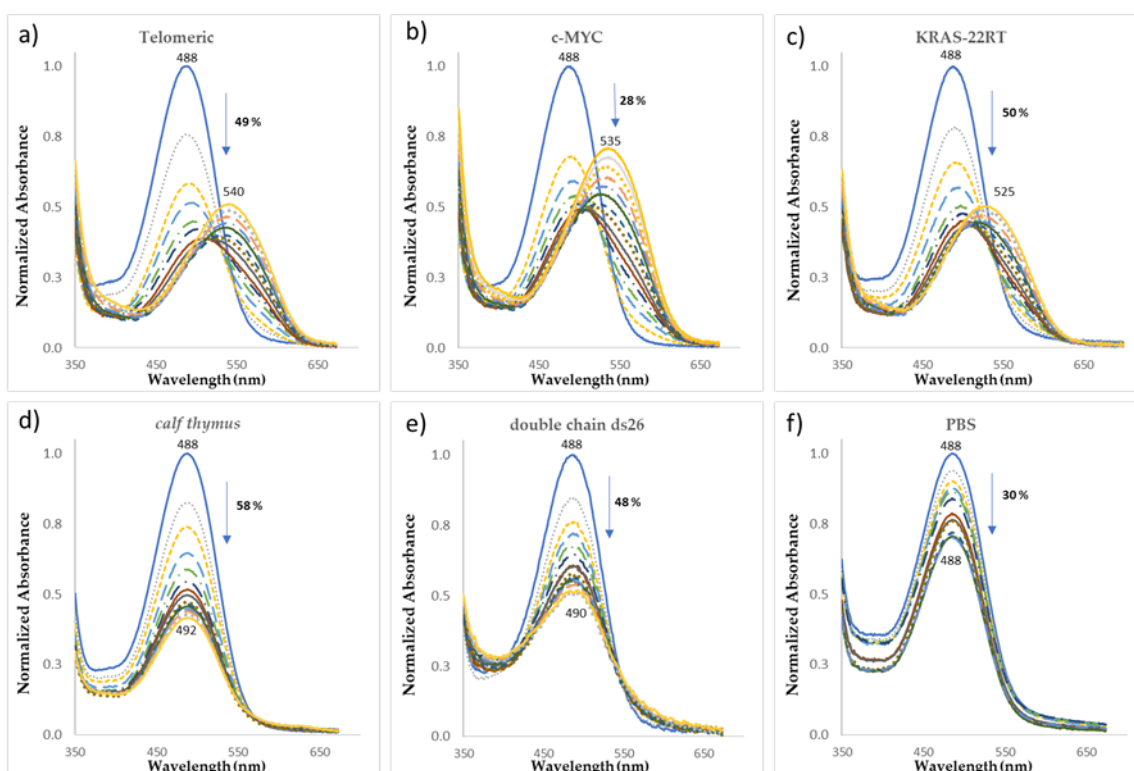

Figure 7 – UV-Vis absorption spectra (350–700 nm) for the titrated solutions of DPP(PyMe)₂ (5.0 µM) with a) telomeric G4, b) c-MYC, c) KRAS-22-RT, d) calf thymus, e) ds26 and f) PBS ; [DNA] = 0 to 4.8 uM.

The most remarkable changes were observed in the presence of G4 DNA sequences with surprisingly high red shifts: 52 nm for the telomeric DNA, 47 nm for c-MYC and 37 nm for KRAS. In contrast, the double-stranded sequences *calf thymus* and ds26 showed insignificant deviations of 2 and 4 nm.

Concerning the observed hypochromic effect (see Figure 7 and Table 3), the most pronounced intensity decreases were observed in the case of telomeric and c-MYC G4 structures that present a maximum hypochromism of 62 and 51%, respectively, and at the end of titrations of 49 and 28%. For the KRAS G4 structure a less pronounced hypochromism of about 50% was observed. In the case of the double stranded DNA, *calf thymus* and ds26, hypochromism of 58% and 48% were observed, respectively.

When the titrations were performed just in the presence of the PBS buffer solution a decrease in the absorbance of 30% was observed. Considering that this decrease in the case of the double strand structures occurred in almost the same wavelength values, between 488 and 492 nm, the hypochromic effect for the double strand structures were corrected by the value observed for PBS. The red shift and hypochromic effect obtained at the end of each individual titration as well as the binding stoichiometry are summarized in table 3.

Table 3 – Red shifts and hypochromic percentages observed with the different DNA structures obtained from UV-Vis titrations

	Telomeric G4	c-MYC	KRAS	*Calf thymus*	ds26	PBS
Red shift (nm)	52	47	37	4	2	0
Hypochromic effect (%)*	62/49	51/28	57/50	28	18	30
Stoichiometry DNA:lig	1G4:2lig	1G4:2lig	1G4:2lig	1ds:1lig	1ds:1lig	--

* In the case of the G4 structures the hypochromic effect maximum and at the end of the titration were presented. For the double stranded structures, the hypochromic percentages were corrected to the one observed when DPP(PyMe)$_2$ was titrated with PBS (30%)

The described behaviour points out to the formation of new species, probably stable adducts DPP(PyMe)$_2$–G4, if the red shift is also considered. The hypochromic effects (28 and 18%) detected in the presence of the double-stranded DNA sequences were accompanied by insignificant shifts ($\Delta\lambda$ = 2 and 4 nm) in the absorbance band of DPP(PyMe)$_2$. The obtained data suggests that DPP(PyMe)$_2$ presents high affinity and interacts strongly with G4 structures and in a selective way. Moreover, the results are highly suggestive of the occurrence of intercalation of DPP(PyMe)$_2$ in the G4 structures, since the observed red shifts were significantly higher than the value of 15 nm usually associated to this type of process.

The binding stoichiometries, DNA:Lig, obtained using the continuous variation approach, of 1G4:3DPP(PyMe)$_2$ and of 1ds:1DPP(PyMe)$_2$ also corroborate the higher affinity of DPP(PyMe)$_2$ for the studied G4 topologies (Table 3).

Along with the red shifts and hypochromic effects observed in the case of the telomeric and c-MYC sequences, it is possible to identify the existence of isosbestic points, that are indicative of the existence of two different species in equilibrium, probably the DPP(PyMe)$_2$ and its adduct with the G4 structure.

3.4 - Fluorescence Studies

3.4.1 - Fluorescence Titrations

The alterations of DPP-PyMe intrinsic fluorescence in the presence of the DNA structures was also used to determine the apparent equilibrium dissociation constants. The spectra obtained from the fluorometric titrations are presented in Figure 8.

Figure 8 - Fluorescence titrations of DPP(PyMe)$_2$ (2.5 uM in PBS) with a) telomeric G4, b) c-MYC, c) KRAS-22-RT, d) *calf thymus*, e) ds26 and f) PBS; [DNA] = 0 to 4.8 uM; λexc = 485 nm

The results show that a pattern of fluorescence quenching was observed in all the performed titrations, but the impact of that quenching was significantly different for the telomeric and oncogene promotors G4s when compared with both double-strandedDNA, ds26 and *calf thymus*. A titration with PBS was also performed not only to correct the observed hypochromic effect (14%) for the DNA structures but also to better understand the effect of the water molecules in the DPP(PyMe)$_2$ molecule, since aggregation processes can also be related to quenching phenomena.

Both oncogene promotor G4 structures, c-MYC and KRAS showed the most pronounced quenching, ca 92% and 88%, respectively, followed by the telomeric sequence with a quenching of 62%. For these three G4s structures a bathochromic effect of 9 nm was also observed. For the *calf thymus* and for the ds26 double-stranded DNA quenching of 55% and 51%, respectively , with no wavelength deviation was observed.

The observed fluorescence intensity quenching is commonly associated to an electron transfer between the excited ligand and DNA structures. Considering that the guanine residues are the most easily oxidized, when compared with the other DNA bases, and the high number of guanines that constitute G4s, this electron transfer process is favourable.[70] Additionally, considering that end-stacking or external binding involving G-quartets is the most common binding site of a large number of ligands, it is not unexpected that binding of many fluorescent ligands comprises an effective quenching of their fluorescence. From these fluorimetric titrations it was possible to calculate the apparent equilibrium dissociation constants (see details in experimental section) for the G4 structures, however, in the case of the double stranded DNA

structures, in the same experimental conditions, the Kd determination was not possible. These results is indicative of a lower affinity of DPP(PyMe)$_2$ to the double stranded DNA structures.

The results summarized in Figure S8 and Table 4 show K_D values in the same range for both DNA structures.

Table 4 - Apparent equilibrium dissociation constants obtained from fluorescence titrations (n.a – non available)

	Telomeric G4	c-MYC	KRAS	*Calf thymus*	ds26
K_D / μM	1.39 ± 0.06	1.22 ± 0.08	0.50 ± 0.01	n.a.	n.a.
DC$_{50}$ / μM	1.52	1.05	1.01	2.77	3.22

3.4.2 - *G4-FID assay*

The high affinity observed for all the selected DNA structures led us to perform the G4 fluorescent intercalator displacement (G4-FID) assay[26] to clarify if the ligand has any selectivity towards G4 or to duplex DNA structures.[22] This assay is based on the loss of fluorescence of a probe like thiazole orange (TO) as a result of its displacement from each DNA sequence by a ligand (see details in the experimental section). The concentration of ligand required to decrease by 50% the probe fluorescence (DC$_{50}$) was determined from the percentage of displacement. The obtained results are compiled in Figure 9, and the DC$_{50}$ values indicated in table 4.
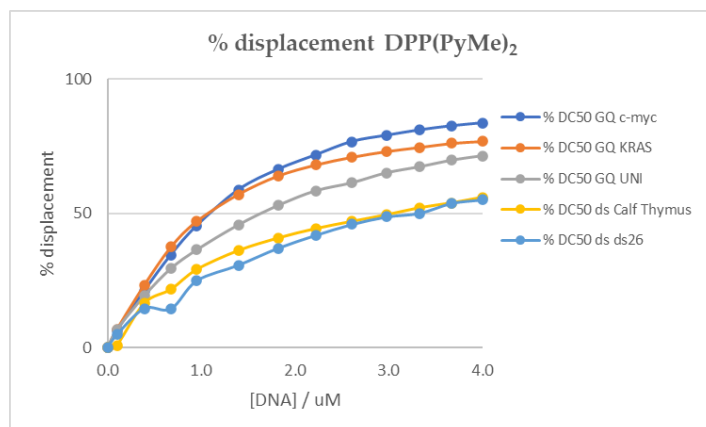
Figure 9 - G4-FID assay performed in PBS at 25 °C for DPP(PyMe)$_2$ and the different DNA structures.

Lower values of D_{C50} were obtained for the G4 structures, in special for the oncogene promotor sequences. A very considerable difference was found for both double-stranded structures in special for ds26 sequence (DC_{50} = 3.22) that was found to be approximately three times higher than the obtained in the case of c-MYC (DC_{50} = 1.02) and KRAS (DC_{50} = 1.05) and more than two times higher than the obtained for the telomeric sequence (DC_{50} = 1.52). The obtained data from these G4-FID assays points to a pattern of selectivity of the ligand to G4 structures that are in agreement with the results obtained from UV-Vis and was validated by the selectivity factor (S) obtained from the FRET melting studies (see below).

The affinity of DPP(PyMe)$_2$ towards G4 structures combined with its pattern of selectivity to these structures is of extreme relevance for targeting of the telomeres, considering the ultimate delivery of the drug at the cellular nucleus where a larger amount of duplex DNA is present. The undesired interaction of the ligand with duplex DNA would reduce its availability as ligand, thus resulting in a reduction of its telomerase inhibition and/or regulatory function.[71]

3.5 - *In silico* studies

A deeper insight into the binding mode of DPP(PyMe)$_2$ and different G4 structures was obtained by molecular docking combined with molecular dynamics studies. The crystal structure of human telomeric DNA dAGGG(TTAGGG)$_3$ (PDB code: 4G0F) and NMR structures of c-MYC (PDB code: 1XAV), KRAS-22RT (PDB code: 5I2V) and KRAS-32R G9T conformer (PDB code: 6SUU) were used as docking models for simulation using Autodock 4.2.6. Each run provided 10 different conformers of the interaction between DPP(PyMe)$_2$ and G4s. A list with the free binding energies for each G4/DPP(PyMe)$_2$ conformer was showed in Table S2. The most energetically favorable binding poses of each G4/DPP(PyMe)$_2$ pair are highlighted in Figure S9. Next, the lowest binding energy conformers (Figure S9) obtained from docking studies were further subjected to molecular dynamic simulations. The conformational stability of the G4/ligand complexes was evaluated by measuring the RMSD during the simulations (Figure S10). The RMSD values of the complexes between the ligand and telomeric and KRAS-22RT G4s indicated that stable complexes were achieved at RMSD values ~0.4-0.5 Å (Figure S10A and S10C). This indicates that the ligand/G4 contacts remained intact after stable complexes were attained. On the other hand, the RMSD plot of the complex c-MYC/ligand showed a significant fluctuation in the first 5 ns (~1 Å), but a stable complex at ~0.5 Å in the remaining simulation time. The RMSD plot of the ligand on KRAS-32R conformer G9T showed a significant fluctuation of the ligand during the first 60 ns. After that, RMSD drop down and a relatively stable RMSD at ~0.6 Å was attained. (Figure S10D). Therefore, from RMSD analysis it is clear that KRAS-32R ligand-binding orientation changed significantly over the first 60 ns of simulation time.

The site-specific binding of the ligand towards G4 structures is depicted in snapshots presented in Figure 10, while the final MD snapshots showing side and top views are shown in Figure S11.

Regarding telomeric G4, the binding mode of the ligand, after 100 ns of simulation, changes from loop/groove binding in the initial docking conformer to stacking mode in the final MD structure (Figure 10A and S11A). In the final structure, the ligand stacks over the top G-tetrad formed by G2-G8-G14-G20. Interestingly, nucleobase A1 stacks over the ligand, which is sandwiched between the top G-quartet and nucleobase A1. The nucleobases A7 and A19 from G4 loops also interact with the ligand.

In the particular case of the complex c-MYC/ DPP(PyMe)$_2$, the final snapshot also showed the stacking of the ligand with the first 5'-end nucleobases and the top G-tetrad (Figure 10B and S11B). Specifically, the ligand interacts on a binding pocket formed by T1 and A3 in the bottom, and G2 on the top forming a cap. Moreover, stacking interactions of the ligand with nucleobases G8 and G13 of c-MYC top G-tetrad were also observed.

The binding mode of the ligand to KRAS-22RT G4 is similar to that obtained from molecular docking experiments. The final snapshot of the molecular dynamic structure showed an end-stacking binding mode of the ligand with the bottom G-tetrad G4-G9-G13-G20 (Figure 10C and S11C). The ligand binds to a cavity between the bottom G-tetrad and nucleobases T8, A21 and A22, which build up a cap over the ligand.

Finally, the ligand binding to the KRAS-32R G4 structure was evaluated. The final snapshot of the molecular dynamic simulation showed the attachment of the ligand on the bottom of the G4 structure (Figure 10D and S11D). The ligand interacts with G29, G31 and G32 by stacking interactions. By creating a cap over the G-tetrad, these three nucleobases seem to hinder the access and interaction of the ligand to the bottom G-tetrad.

Altogether, these results are in agreement with the data obtained from UV-Vis and fluorescence spectroscopy, suggesting that the ligand interacts with the G4s mainly via $\pi-\pi$ stacking interactions. Indeed, the large aromatic nature of the ligand favours stacking interactions with outer G-tetrads. However, the

high flexibility of the side chains also permits interactions of the ligand with the loop nucleobases. Several G4 binders have been reported as interacting with the G4s mainly by π–π stacking interactions. For instance, the binding of TMPyP4 to different human telomeric G4 topologies has been studied.[72] The results showed that TMPyP4 binds most efficiently with the parallel G4 topology due to the prevalence π–π stacking interaction of the G-quartets with the aromatic moieties of the ligand. Nevertheless, TMPyP4 also establishes interactions with G4 grooves and charged backbone by positively charged N-methylpyridinium side chains. In the last few years, several studies have reported the synthesis and development of G4 probes.[73] These studies showed that in many cases, π–π stacking interactions are the main driving forces for ligand/G4 interactions. For instance, the G4 optical probe IZFL-2, which specifically recognize c-MYC G4, was characterized by experimental and *in silico* methods. The results revealed that π–π stacking interaction significantly contribute to the binding of the ligand towards c-MYC G4.[74]
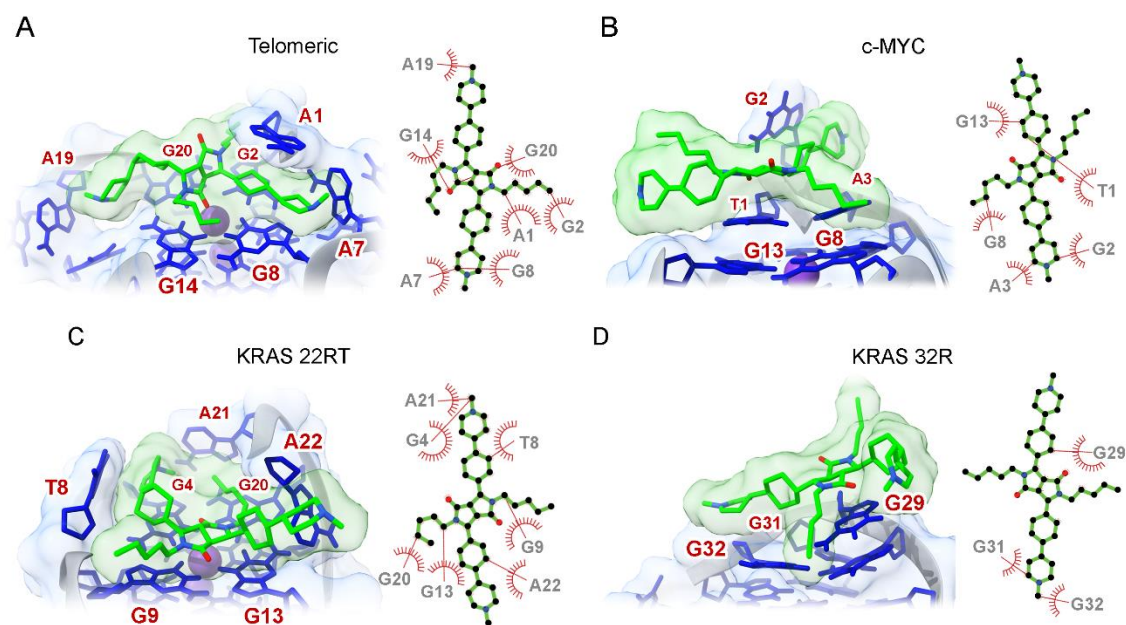

Figure 10. Final snapshots of molecular dynamic simulations and 2D diagram representations showing the binding site of DPP(PyMe)₂ in (A) telomeric, (B) c-MYC, (C) KRAS-22RT and (D) KRAS-32R conformer G9T G4. G4 structures are

highlighted in blue with K$^+$ cations depicted as purple spheres, while nucleobases are highlighted in red.

3.6 - FRET melting studies

The FRET melting assay was also used to validate the binding and stabilisation of DPP(PyMe)$_2$ towards G4 structures.[75,76] The experiments were carried out with G4 oligonucleotides as well as a duplex sequence d(TATAGCTAT-hexaethyleneglycol-TATAGCTATA) labelled in 5′ and 3′ with FAM and TAMRA (FdxT) in order to assess the selectivity of DPP(PyMe)$_2$ ligand.. The G4 sequences used are localised at telomere ends and in oncogene promotors such as, c-MYC and KRAS. The data highlighted promisor stabilising effects of the ligand in the G4 sequences. The results are depicted in Table 5 and show the ΔT_m values of oligonucleotides in the absence and presence of increasing ligand concentrations.

The results suggest that the ligand is selective towards G4 over duplex DNA, as a small stabilisation of the duplex was observed for DDP(PyMe)$_2$ ligand at 8 molar eq. (ΔT_m of 2.5 °C).

Table 5. DPP(PyMe)$_2$-induced thermal stabilisation measured by FRET melting experiments.

Ligand	ΔT_m [a] (°C)			
	1 molar Eq.	2 molar Eq.	4 molar Eq.	8 molar Eq.
FdxT[b]	-	-	0.5 ± 0.1	2.5 ± 0.4
FmycT[c]	0.6 ± 0.1	2.3 ± 0.1	11.5 ± 0.9	20.5 ± 0.7
FKRAS32R[d]	0.6 ± 0.2	2.0 ± 0.6	7.2 ± 1.9	16.6 ± 2.1
FKRAS22RT[d]	1.0 ± 0.3	6.1 ± 1.6	11.2 ± 0.6	15.6 ± 0.4
FtelomericT[d]	0.6 ± 0.3	3.3 ± 0.7	9.2 ± 1.8	13.6 ± 1.7

[a]ΔT_m represents the difference in melting temperature of oligonucleotides (0.2 μM) in the

presence of different molar equivalents of DPP(PyMe)$_2$. The buffer used was 10 mM lithium cacodylate pH 7.2 supplemented with [b] 100 mM KCl; [c] 1 mM KCl and 99 mM lithium chloride and [d] 10 mM KCl and 90 mM lithium chloride.

Next, the impact of a non-G4 competitor sequence on the stabilisation of G4 structures was evaluated. A FRET melting competition assay was performed in the presence of 4 molar eq. of the ligand and an excess of ds26 (3 and 10 μM). Furthermore, the selectivity factor (*S* factor) was determined and relies on the relative stabilisation of DPP(PyMe)$_2$ remaining in the presence of 3 and 10 μM of the ds26 sequence.[55] The results are depicted in Table 6 and show that ds26 is an ineffective competitor of G4 sequences. The *S* factors determined for the G4 sequences were near to 1 in the presence of 10 μM of ds26 (50 molar eq.). A value of *S* factor closer to 1 means that the binding of the ligand to ds26 is almost negligible.[55] Overall, the results showed that DPP(PyMe)$_2$ can be selective for G4 structures in the presence of ds26.

Table 6. FRET melting stabilisation of G4 sequences by DPP(PyMe)$_2$ (0.8 μM) in the presence of increasing concentrations of ds26 (0, 15 and 50 molar eq.). *S* factor values for each G4 sequence in the presence of ds26 (15 and 50 molar eq.) are depicted.

	ΔT_m (°C)[a]			*S* factor	
	Ligand	Ligand and 15 molar eq. ds26	Ligand and 50 molar eq. ds26	Ligand and 15 molar eq. ds26	Ligand and 50 molar eq. ds26
FmycT[b]	11.5	10.8	11.5	0.94	1
FKRAS32RT[c]	7.2	5.4	6.6	0.75	0.91
FKRAS22RT[c]	11.2	11.0	11.3	0.98	>1
FtelomericT[c]	9.2	9.4	8.7	>1	0.95

[a] ΔT_m represents the difference in melting temperature of oligonucleotides (0.2 μM) in the presence of 4 molar equivalents of DPP(PyMe)$_2$ (4 molar eq.). The buffer used was 10 mM lithium cacodylate pH 7.2 supplemented with [b] 1 mM KCl and 99 mM lithium chloride and [c] 10 mM KCl and 90 mM lithium chloride.

3.7 - Circular dichroism experiments

CD titrations were further used to assess the ability of DPP(PyMe)$_2$ to bind and promote conformational changes on the oncogene G4 structures c-MYC and KRAS (KRAS 32R and KRAS 22RT). The CD spectra were acquired in the absence and presence of increasing concentrations of the ligand (Figure 11). Upon titration of the G4 structures with the ligand, no significant changes were observed in the characteristic bands of G4 structures (positive band ~ 260 nm and negative band ~ 240 nm). In general, the results of CD titrations revealed that ligand binds and preserves the G4 structures but does not change the initial parallel stranded topology. On the other hand, the telomeric sequence in a K$^+$ rich solution forms a mixed (3 + 1) hybrid-type G4 structure (positive bands ~ 291 and 255 nm and negative band ~ 230 nm).[77,78,79] The addition of increasing concentrations of the ligand leads to an increase in CD band at 262 nm at the expense of the band at 291 nm. Overall, the ligand could trigger topology switching to the parallel topology from the hybrid-type G4 structure.[80] A similar effect was previously observed by Yatsunyk et al. that showed the ability of N-methyl mesoporphyrin IX to induce the parallel structure when the sequence is annealed in the presence of ligand in potassium buffer.[79] Other G4 ligands such as, the carbazole derivative BPBC[81] or the oxazole derivative DR4-47[82] also showed ability to induce such conformational remodelling of the telomeric G4 structure.
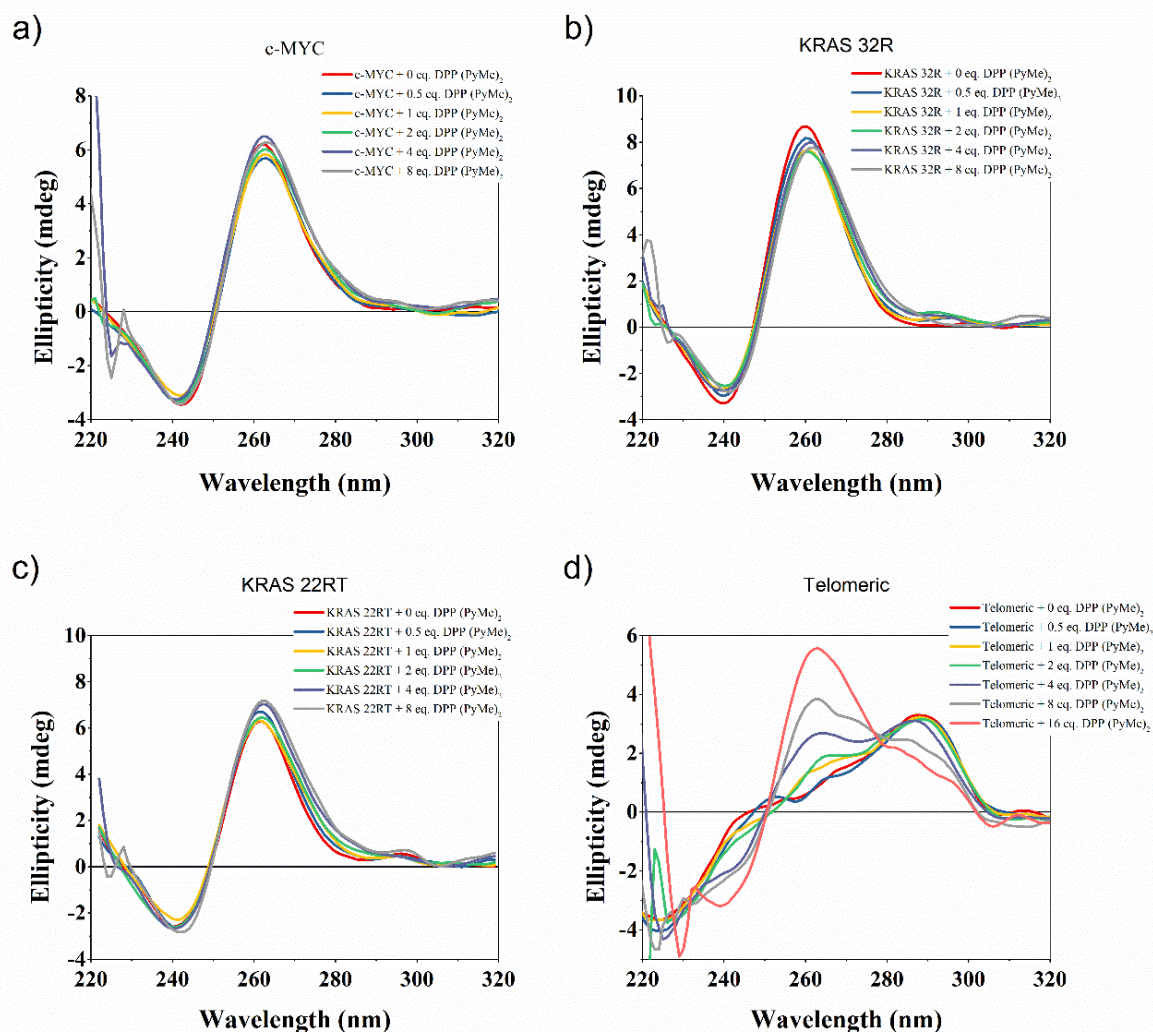
Figure 11. CD titration spectra of **(A)** c-MYC (1 mM KCl and 99 mM LiCl), **(B)** KRAS 32R, KRAS 22RT and **(D)** 22AG (10 mM KCl and 90 mM LiCl) in the absence and presence of increased concentrations of DPP(PyMe)$_2$.

The influence of ligand on the thermal stability of G4 structures was also assessed by using CD melting experiments. Firstly, the G4 structures in PBS solution were adjusted for melting temperature. The ellipticity of promotor G4 structures was monitored at 262 nm, whereas the ellipticity of the telomeric G4 structure was monitored at 291 nm (Figure 12). The melting temperatures for c-MYC, KRAS 32R, KRAS 22RT and telomeric sequences were 59.2, 62.1, 48.3 and 61.0 °C, respectively. Upon addition of 8 molar equivalents of the ligand, the c-MYC and KRAS 22RT G4 structures were stabilized in more than 30 °C, while

the KRAS 32R G4 structure is stabilized in a less extent way (ΔT_m of 21.2 °C). We hypothesize that this difference in thermal stability G4 structures could be attributed to the different length of oligonucleotides, molecularity, and polymorphism propensity.[83] Recently, it was reported the formation of the dimeric forms of c-MYC and KRAS 22RT G4 sequences[84,85] but was not found evidence for the formation of a dimer complex in the wild-type sequence of KRAS 32R.[86] Furthermore, Salgado et al. proved by NMR spectroscopy that the KRAS 32R sequence can fold into two different G4 conformations. Other studies performed on KRAS G4 sequences also suggested the presence of two conformations of KRAS 32R with very different melting temperatures.[83,87] For instance, Cogoi et al. also suggested the presence of two conformations (parallel and antiparallel) of KRAS 32R with very different melting temperatures.[87]

The addition of the ligand to the telomeric G4 structure did not render significant changes in the melting temperature. It is worth mentioning, however, that this stabilization temperature is calculated relative to melting temperature of the hybrid-type topology of telomeric sequence as in the absence of ligand the sequence does not adopt a parallel topology and CD band at 262 nm does not display temperature dependence.

Altogether, these pieces of evidence suggest that the ligand seems to have a greater thermal effect on G4s with parallel topology.
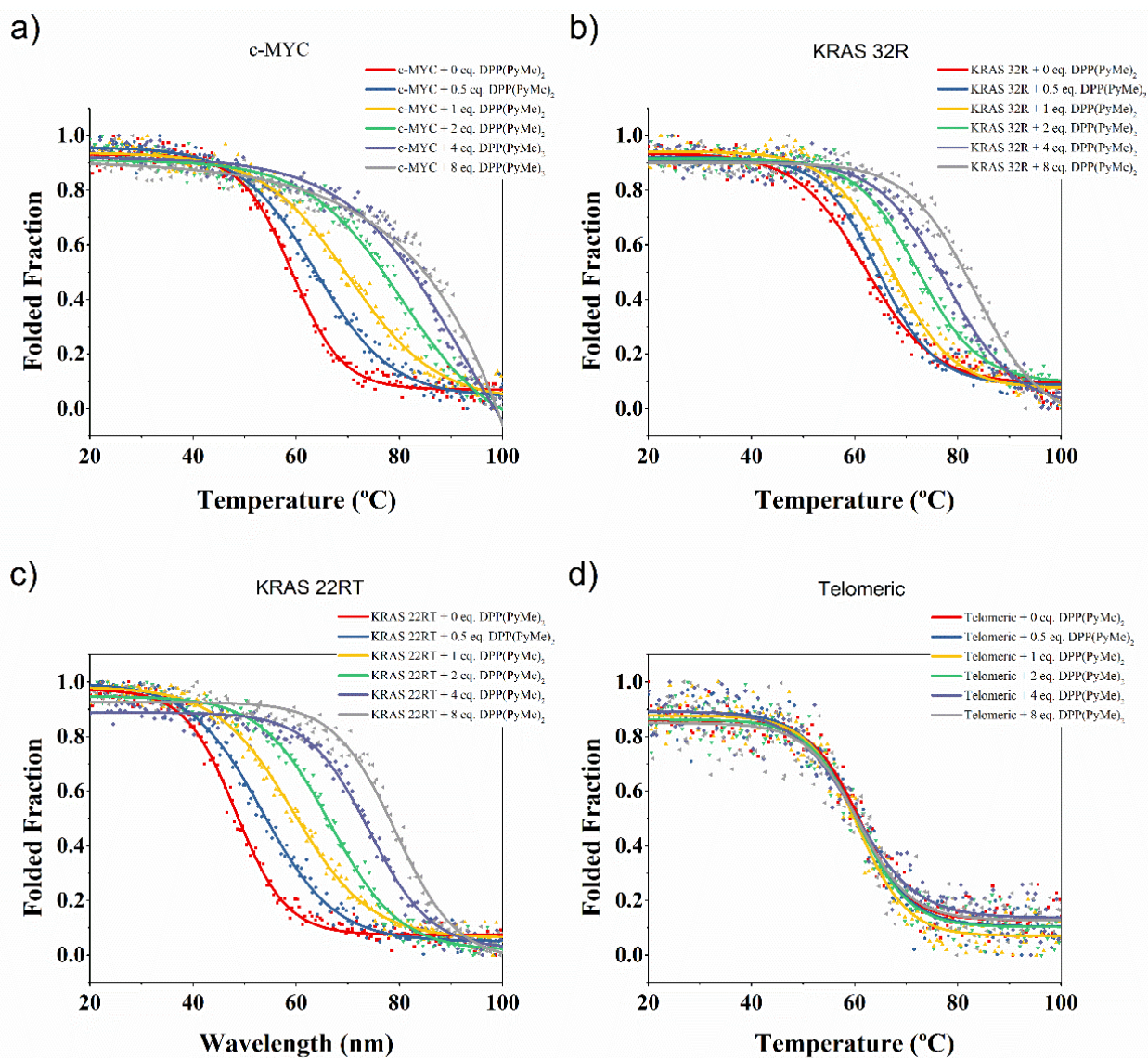
Figure 12. CD melting spectra of **(A)** c-MYC (1 mM KCl and 99 mM LiCl), **(B)** KRAS 32R, **(C)** KRAS 22RT and **(D)** 22AG (10 mM KCl and 90 mM LiCl) in the absence and presence of increased concentrations of DPP(PyMe)$_2$.

3.8 - PCR stop assay

Once CD and FRET-melting experiments revealed that DPP(PyMe)$_2$ stabilizes in a higher extension the c-MYC G4 structure over the KRAS 32R, the ability of DPP(PyMe)$_2$ in blocking the biological activity of *Taq* polymerase was investigated by means of PCR stop assay[25,88] using only c-MYC G4. Sequences of

the Pu77 G4 (c-MYC) and Pu77-mut (c-MYC mutated) and the corresponding complementary sequence (RevPu77) (Table 2) were incubated with increasing concentrations of the ligand for 30 PCR cycles. The results are highlighted in Figure 13. In the presence of 4 molar equivalents of the ligand, Pu77 extension with *Taq* polymerase was partially inhibited and the final double-stranded DNA PCR product was less detectable than in the lane without ligand (Figure 13A). Conversely, Pu77-mut sequence, which has mutations in the G-repeats, remains almost unaffected in the presence of the ligand (Figure 13B). Even at higher concentrations (16 and 32 molar equivalents) of the ligand the band of the final PCR product remains well-defined and visible. In the presence of 32 molar equivalents, the final double-stranded DNA PCR product was not observed and only a small smear is detected. Indeed, it is possible to observe that the final PCR product was inhibited in a dose-dependent manner.
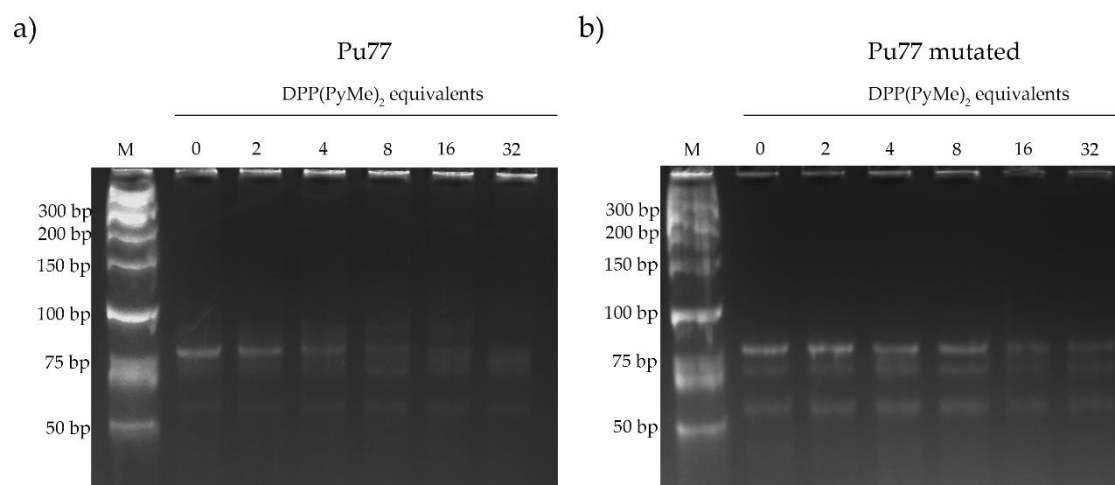

Figure 13. Polyacrylamide gel electrophoresis of **(A)** Pu77 G4 and **(B)** Pu77-mut in the presence of increased concentrations of DPP(PyMe)$_2$ (0 μM, 0.8 μM, 1.6 μM, 3.2 μM and 6.4 μM and 12.8 μM).

3.9 - Colocalization studies

Once the ligand has intrinsic fluorescence properties, confocal microscopy was employed to assess its subcellular localization. The results are highlighted in Figure 14. After treating HeLa cells with the ligand for 45 min,

the DPP(PyMe)$_2$ seems to be localized in the cytoplasm and partially in the nucleus/nucleolus (Figure 14B). A more modest uptake of DPP(PyMe)$_2$ was detected in the cytoplasm of NHDF cells and the ligand was not detected in the nucleus/nucleolus, which suggests tumour-selective properties of the ligand (Figure 14A). This interesting feature makes the ligand attractive for the development of G4 labelling probes.
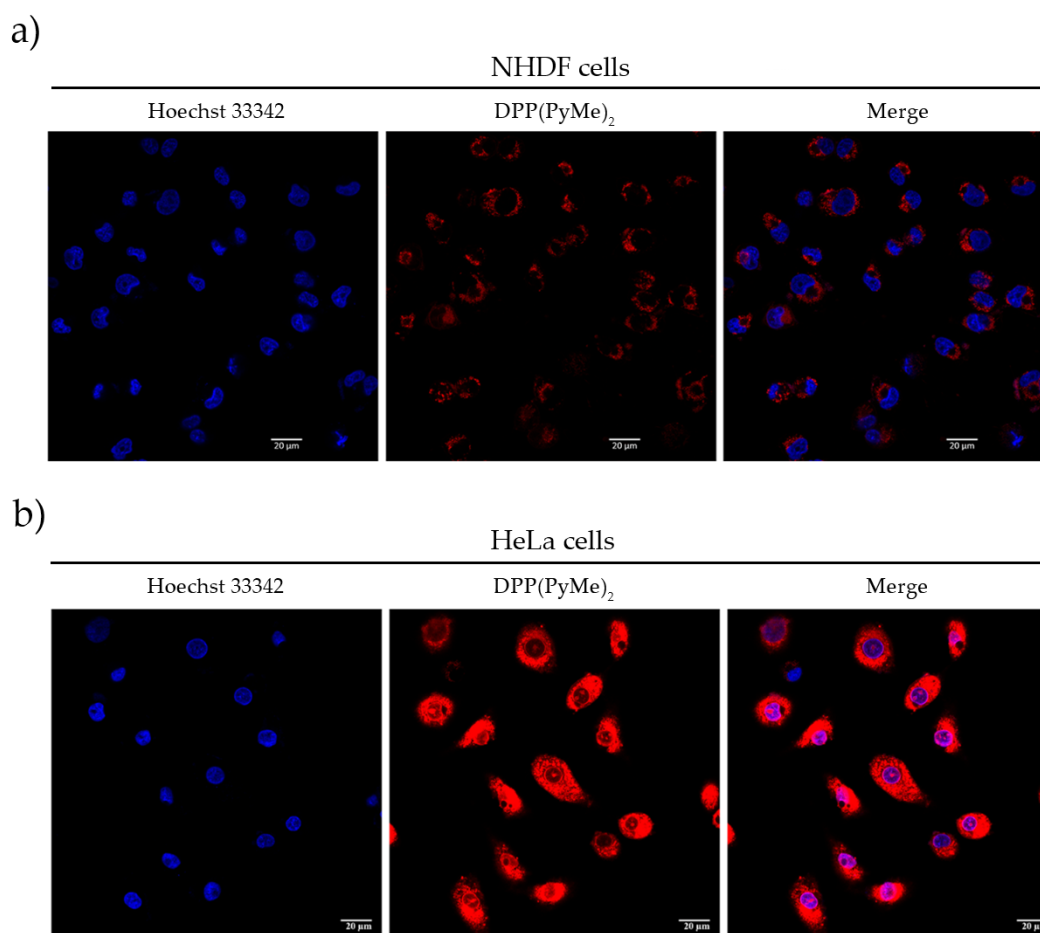
a)

b)

Figure 14. Confocal microscopy images of **(A)** NHDF and **(B)** HeLa cells treated for 45 min with 10 µM DPP(PyMe)$_2$ (middle). Nuclear probe Hoechst 33342 (1 µM, left) was used for colocalization (merge, right). Scale bar is 20 µM.

4 – Conclusions

An efficient synthetic strategy was developed to obtain the novel dicationic DPP derivative (DPP(PyMe)$_2$, with a planar structure and with high capacity to stablish strong π–π stacking interactions with G4s.

The data obtained from the spectroscopic analysis corroborate that the ligand DPP(PyMe)$_2$ presents a high affinity towards G4 structures, and is particularly selective for oncogene promotors.

The results of MD simulations revealed that DPP(PyMe)$_2$ binds to G4s mainly by π–π stacking interactions. These results agree with the data obtained from the UV-Vis and fluorescence spectroscopy (high hypochromism and efficient fluorescence quenching of G4s), which indicated the binding of the ligand towards G4s mainly through an end-stacking mode, akin to that observed for other G4/ligand complexes. Altogether, these results are in line with the binding mode observed for G4 binders with a large aromatic surface.

CD and FRET melting experiments validate that DPP(PyMe)$_2$ has selectivity for G4s in the presence of ds26. CD titrations revealed that, upon addition of 8 molar equivalents of the ligand, a stabilization higher than 30 °C in the case of c-MYC G4 structure and of about 21.2 °C for the KRAS 32R G4 occurs. Once again, these results are in agreement with MD simulations, where KRAS 32R established fewer contacts with the ligand, suggesting less potential of the ligand to bind and stabilize the G4 structure. The results obtained by CD titrations also showed that DPP(PyMe)$_2$ switch the topology of telomeric G4 from a hybrid to a parallel type G4. Furthermore, the results from CD-melting studies suggest a strong preference of DPP(PyMe)$_2$ for parallel G4 structures.

From the PCR stop assay results, it was possible to demonstrate that DPP(PyMe)$_2$ has the ability to block the activity of *Taq* polymerase in a dose-dependent manner, in the case of the c-MYC sequence. The subcellular

localization obtained with confocal microscopy corroborates the results obtained by the other techniques.

In the last few years, a range of G4 optical probes has been developed to recognize G4s selectively.[73] Indeed, DPP derivatives constitute a class of pigments covering a colour range from yellow-orange to dark violet, which open up a new framework to develop novel G4 fluorescent probes.

In conclusion, the data here reported suggest that DPP(PyMe)$_2$ is an attractive ligand for the development of G4 labelling probes.

References

[1] J. Nandakumar, T.R. Cech, Finding the end: recruitment of telomerase to the telomere, Nat Rev Mol Cell Biol. 14 (2013) 69-82, https://doi: 10.1038/nrm3505

[2] Y. Chen, Y. Zhang, Functional and mechanistic analysis of telomerase: An antitumor drug target, Pharmacol Ther. 163 (2016) 24-47, https://doi: 10.1016/j.pharmthera.2016.03.017

[3] T. M. Bryan. Mechanisms of DNA Replication and Repair: Insights from the Study of G-Quadruplexes. Molecules. *24* (2019), 3439. https://doi.org/10.3390/molecules24193439

[4] S. Neidle, Quadruplex nucleic acids as novel therapeutic targets, J. Med. Chem. 16 (2016) 5987 -6011, https://doi: 10.1021/acs.jmedchem.5b01835

[5] G.W. Collie, G.N. Parkinson, The application of DNA and RNA G-quadruplexes to therapeutic medicines, Chem. Soc. Rev. 40 (2011) 5867-5892, https://doi.org/10.1039/C1CS15067G

[6] A. De Cian, L. Lacroix, C. Douarre *et al.* ,Targeting telomeres and telomerase, Biochimie 90, (2008) 131-155, https://doi: 10.1016/j.biochi.2007.07.011

[7] A. L. Moye, K.C. Porter, S. B. Cohen, T. Phan *et al.*, Telomeric G-quadruplexes are a substrate and site of localization for human telomerase, Nat. Commun. 6 (2015) 7643, https://www.nature.com/articles/ncomms8643

[8] Y. Qin, L.H. Hurley, Structures, folding patterns, and functions of intramolecular DNA G-quadruplexes found in eukaryotic promoter regions, Biochimie. 90 (2008) 1149-1471, https://doi: 10.1016/j.biochi.2008.02.020.

[9] J. L. Huppert, S. Balasubramanian. G-quadruplexes in promoters throughout the human genome. Nucleic Acids Research 35 (2007) 406–413, https://doi.org/10.1093/nar/gkl1057

[10] E. Besnard, A. Babled, L. Lapasset, O. Milhavet, H. Parrinello, C. Dantec, J. M. Marin, J. M. Lemaitre. Unraveling cell type-specific and reprogrammable human replication origin signatures associated with G-quadruplex consensus motifs. Nat Struct Mol Biol. 19 (2012) 837-844. https://doi:10.1038/nsmb.2339

[11] J. L. Huppert, A. Bugaut, S. Kumari, S. Balasubramanian. G-quadruplexes: the beginning and end of UTRs. Nucleic Acids Res 36 (2008) 6260–6268. https://doi:10.1093/nar/gkn511

[12] M. Lexa, P. Steflova, T. Martinek, M. Vorlickova, B. Vyskot, E. Kejnovsky Guanine quadruplexes are formed by specific regions of human transposable elements. BMC Genomics. 15 (2014):1032. https://doi: 10.1186/1471-2164-15-1032

[13] P. Mani, V. K. Yadav, S. K. Das, S. Chowdhury. Genome-wide analyses of recombination prone regions predict role of DNA structural motif in recombination. PLoS One. 4(2009) e4399. https://doi:10.1371/journal.pone.0004399

[14] W. M. Guiblet, M. DeGiorgio, X. Cheng, F. Chiaromonte, K. A. Eckert, Y. F. Huang, K. D. Makova. Selection and thermostability suggest G-quadruplexes are novel functional elements of the human genome. Genome Res. 31 (2021) 1136–49. https://doi: 10.1101/gr.269589.120.

[15] D. Varshney, J. Spiegel, K. Zyner, D. Tannahill, S. Balasubramanian. The regulation and functions of DNA and RNA G-quadruplexes. Nat Rev Mol Cell Biol. 21(2020) 459-474. https://doi:10.1038/s41580-020-0236-x

[16] A. Siddiqui-Jain, C.L. Grand, D. J. Bearss, L. H. Hurley. Direct evidence for a G-quadruplex in a promoter region and its targeting with a small molecule to repress c-MYC transcription. Proc. Natl. Acad. Sci. U.S.A. 99 (2002), 11593–11598 https://doi.org/10.1073/pnas.182256799

[17] S. Kumari, A. Bugaut, J. L. Huppert, S. Balasubramanian. An RNA G-quadruplex in the 5 UTR of the NRAS proto-oncogene modulates translation. Nat. Chem. Biol. 3 (2007) 218–221 https://doi: 10.1038/nchembio864

[18] E. D. Larson, M. L. Duquette, W. J. Cummings, R. J. Streiff, N. Maizels. MutSalpha binds to and promotes synapsis of transcriptionally activated immunoglobulin switch regions. Curr. Biol. 15 (2005) 470–474. https://doi :10.1016/j.cub.2004.12.077

[19] W. Yoshida, T. Saito, T. Yokoyama, S. Ferri, K. Ikebukuro. Aptamer selection based on G4-forming promoter region. PLoS One. 8 (2013) e65497. https://doi.org/10.1371/journal.pone.0065497

[20] V. Marcel,P. L. T. Tran, C. Sagne, G. Martel-Planche, et al. G-quadruplex structures in TP53 intron 3: Role in alternative splicing and in production of p53 mRNA isoforms. Carcinogenesis. 32 (2011) 271–278. https://doi.org/10.1093/carcin/bgq253

[21] M. Jara-Espejo, S. Roberto Line. DNA G-quadruplex stability, position and chromatin accessibility are associated with CpG island methylation. FEBS 287 (2020) 483–495 https://doi.org/10.1111/febs.15065

[22] P. Murat, Y. Singh, E. Defrancq, Methods for investigating G-quadruplex DNA / ligand interactions, Chem Soc Rev. 40 (2011) 5293, https://doi.org/10.1039/C1CS15117G

[23] Z.Y. Sun, X.N. Wang, S.Q. Cheng, X.X. Su, T.M. Ou, Developing Novel G-Quadruplex Ligands: from Interaction with Nucleic Acids to Interfering with Nucleic Acid‑Protein Interaction, Molecules 24 (2019) 396, https://doi.org/10.3390/molecules24030396

[24] J. Jaumot, R. Gargallo, Experimental methods for studying the interactions between G-quadruplex structures and ligands, Curr. Pharm. Des. 18 (2012) 1900-1916, https://doi.org/10.2174/138161212799958486

[25] J. Carvalho, T. Quintela, N.M. Gueddouda, A. Bourdoncle, J.-L. Mergny, G.F. Salgado, J.A. Queiroz, C. Cruz, Phenanthroline polyazamacrocycles as G-quadruplex DNA binders, Org. Biomol. Chem. 16 (2018) 2776-2786. https://doi.org/10.1039/C8OB00247A

[26] E. Largy, F. Hamon, M.-P. Teulade-Fichou, Development of a high-throughput G4-FID assay for screening and evaluation of small molecules binding quadruplex nucleic acid structures, Anal Bioanal Chem. *400* (2011) 3419-3427, https://doi.org/10.1007/s00216-011-5018-z

[27] A. Marchand, D. Strzelecka, V. Gabelica, Selective and Cooperative Ligand Binding to Antiparallel Human Telomeric DNA G-Quadruplexes, Chem. Eur. J. 22 (2016) 9551-9555, https://doi.org/10.1002/chem.201601937

[28] C.I.V. Ramos, M.G. Santana-Marques, J.P.C. Tomé, Charge and substituent effects on the stability of porphyrin/G-quadruplex adducts, J. Mass Spectrom. 47 *(*2012) 173-179, https://doi.org/10.1002/jms.2048

[29] A. Casagrande, A. Alvino, G. Bianco, O.M. Franceschin, Study of binding affinity and selectivity of perylene and coronene derivatives towards duplex and quadruplex DNA by ESI-MS, J. Mass Spectrom. 44 *(*2009) 530-540, https://pubmed.ncbi.nlm.nih.gov/19034888/

[30] M.J. Lecours, A. Marchand, A. Anwar, C. Guetta, W.S. Hopkins, V. Gabelica, What stoichiometries determined by mass spectrometry reveal about the ligand binding mode to G-

quadruplex nucleic acids, Biochimica et Biophysica Acta 1861 *(*2017) 1353-1361, https://pubmed.ncbi.nlm.nih.gov/28087374/

[31] C.I.V. Ramos, A.R. Monteiro, N.M.M. Moura, Lourenco, M.A.F. Faustino, T. Trinadade, M.G.P.M.S. Neves, The Interactions of H2TMPyP, Analogues and Its Metal Complexes with DNA G-Quadruplexes - An Overview, Biomolecules, 11 (2021) 1404-1432, https://doi.org/10.3390/biom11101404

[32] Georgiades S.N., Karim N.H. A., Suntharalingam K., Vilar R. Interaction of Metal Complexes with G-Quadruplex DNA, Angew. Chem. Int. Ed. 49 (2010) 4020-4034, https://pubmed.ncbi.nlm.nih.gov/20503216/

[33] Ou T.-m., Lu Y.-j., Tan J., Huang Z., Wong K., Gu L., G-Quadruplexes: targets in anticancer drug design, ChemMedChe. 3 (2008) 690-713 https://pubmed.ncbi.nlm.nih.gov/18236491/

[34] K. Shin-ya, K. Wierzba, K. Matsuo, T. Ohtani, Y. Yamada, K. Furihata, Y. Hayakawa, H. Seto, Telomestatin, a novel telomerase inhibitor from *treptomyces anulatus*, Journal of the American Chemical Society. 23 (2001) 1262–1263, https://doi.org/10.1021/ja005780q

[35] D. Monchaud, A. Granzhan , N. Saettel, A. Guédin, J.L..Mergny, M.P. Teulade-Fichou, One ring to bind them all-part I: the efficiency of the macrocyclic scaffold for g-quadruplex DNA recognition, J Nucleic Acids. 2010 (2010), https://doi.org/10.4061/2010/525862

[36] S. Müller, D.A.Sanders, M. Di Antonio, S. Matsis, J.F. Riou, R. Rodriguez, S. Balasubramanian, Pyridostatin analogues promote telomere dysfunction and long-term growth inhibition in human cancer cells, Org. Biomol. Chem. 10 (2012) 6537-6546, https://doi.org/10.1039/C2OB25830G

[37] D. Sun, B. Thompson, B.E. Cathers, M. Salazar, S.M. Kerwin, J.O. Trent, T.C. Jenkins, S. Neidle, L.H. Hurley, Inhibition of Human Telomerase by a G-Quadruplex-Interactive Compound, J. Med. Chem. 40 (1997) 2113–2116, https://doi.org/10.1021/jm970199z

[38] M. Read, R.J. Harrison, B. Romagnoli, F.A.Tanious, S.H. Gowan, A.P. Reszka, W.D. Wilson, L.R. Kelland, S. Neidle, Structure-based design of selective and potent G-quadruplex-mediated telomerase inhibitors, Proc. Natl. Acad. Sci. 98 (2001) 4844-4849, https://pubmed.ncbi.nlm.nih.gov/11309493/

[39] D. Monchaud, M.-P. Teulade-Fichou, A hitchhiker's guide to G-quadruplex ligands, Org. Biomol. Chem. 6 (2008) 627-636, https://doi.org/10.1039/B714772B

[40] R. J. Harrison, S.M. Gowan, L.R. Kelland, S. Neidle, Human telomerase inhibition by substituted acridine derivatives, Bioorg. Med. Chem. Lett. 9 (1999) 2463-2468, https://pubmed.ncbi.nlm.nih.gov/10498189/

[41] J. Carvalho, E. Pereira, J. Marquevielle, M.P.C. Campello, J.L. Mergny, A. Paulo, G.F. Salgado, J.A. Queiroz, C. Cruz, Fluorescent light-up acridine orange derivatives bind and stabilize KRAS-22RT G-quadruplex, Biochimie. 144 (2018) 144-152, https://doi.org/10.1016/j.biochi.2017.11.004

[42] N.H. Campbell, M. Patel, A.B. Tofa, R. Ghosh, G.N. Parkinson, S. Neidle, Selectivity in ligand recognition of G-quadruplex loops, Biochemistry. 48 (2009) 1675-1680, https://doi.org/10.1021/bi802233v

[43] J. Schmitt, V. Heitz, A. Sour, F. Bolze, P. Kessler, L. Flamigni, B. Ventura, C. S. Bonnet, É. Tõth, A Theranostic Agent Combining a Two-Photon-Absorbing Photosensitizer for Photodynamic

Therapy and a Gadolinium(III) Complex for MRI Detection, Chem. - A Eur. J. 22 (2016) 2775–2786, https://doi.org/10.1002/chem.201503433

[44] J. Schmitt, V. Heitz, A. Sour, F. Bolze, H. Ftouni, J. F. Nicoud, L. Flamigni, B. Ventura, Diketopyrrolopyrrole-porphyrin conjugates with high two-photon absorption and singlet oxygen generation for two-photon photodynamic therapy, Angew. Chemie - Int. Ed. 54 (2015) 169–173, https://doi.org/10.1002/anie.201407537

[45] M.L. Agazzi, V.A.S. Almodovar, N.S. Gsponer, S. Bertolotti, A. C. Tomé, E.N. Durantini, Diketopyrrolopyrrole-fullerene C60 architectures as highly efficient heavy atom-free photosensitizers: Synthesis, photophysical properties and photodynamic activity, Org. Biomol. Chem., 18 (2020) 1449–1461, https://pubs.rsc.org/en/content/articlehtml/2020/ob/c9ob02487e

[46] H. Shi, W. Sun, Q. Wang, G. Gu, W. Si, W. Huang, Q. Zhang and X. Dong, A Thienyl-Substituted Diketopyrrolopyrrole Derivative with Efficient Reactive Oxygen Species Generation for Photodynamic Therapy, ChemPlusChem. 81 (2016) 515–520, https://doi.org/10.1002/cplu.201600101

[47] Y. Cai, P. Liang, Q. Tang, X. Yang, W. Si, W. Huang, Q. Zhang, X. Dong, Diketopyrrolopyrrole-Triphenylamine Organic Nanoparticles as Multifunctional Reagents for Photoacoustic Imaging-Guided Photodynamic/Photothermal Synergistic Tumor Therapy, ACS Nano. 11 (2017) 1054–1063, https://doi.org/10.1021/acsnano.6b07927

[48] S. Lin, S. Liu, H. Zou, W. Zeng, L. Wang, R. Beuerman, D. Cao, Synthesis of diketopyrrolopyrrole-containing conjugated polyelectrolytes for naked-eye detection of DNA, J. Polym. Sci., Part A: Polym. Chem. 49 (2011) 3882–3889, https://doi.org/10.1002/pola.24829

[49] S. Lin, S. Liu, F. Ye, L. Xu, W. Zeng, L. Wang, L. Li, R. Beuerman, D. Cao, Sensitive detection of DNA by hyperbranched diketopyrrolopyrrole-based conjugated polyelectrolytes, Sens. Actuators, B, 182 (2013) 176–183, https://doi.org/10.1016/j.snb.2013.02.092

[50] A.R. Monteiro, C.I.V. Ramos, S. Fateixa, N.M.M. Moura, M.G.P.M.S. Neves, T. Trindade, Hybrids based on g raphene oxide and porphyrin as a tool for detection and stabilization of DNA G-quadruplexes, ACS Omega, 3 (2018) 11184 https://doi.org/10.1021/acsomega.8b01366

[51] C.I.V. Ramos, S.P. Almeida, L.M.O. Lourenco, P.M.R. Pereira, R. Fernandes, M.A.F. Faustino, J.P.C. Tome, J. Carvalho, C. Cruz, M.G.P.M.S. Neves, Multicharged phthalocyanines as selective ligands for G-Quadruplex DNA structures, Molecules. 24 (2019) 733-756, https://doi.org/10.3390/molecules24040733

[52] J. Lopes-Nunes, J. Carvalho, J. Figueiredo, C.I.V. Ramos, L.M.O. Lourenço, J.P.C. Tomé, M. G.P.M.S.Neves, J.-L. Mergny, J.A. Queiroz, G.F. Salgado, C. Cruz, Phthalocyanines for G-quadruplex aptamers binding, Bioorganic Chem. 100 (2020) 103920,

https://doi.org/10.1016/j.bioorg.2020.103920

[53] W.L.F. Armarego, C.L.L. Chai. Butterworth-Heinemann (Ed.), Purification of laboratory chemicals (Seventh.), Elsevier, Oxford (2013)

[54] N. Nagesh, V.K. Sharma, A.G. Kumar, E.A. Lewis, Effect of ionic strength on porphyrin drugs interaction with quadruplex DNA formed by the promoter region of C-myc and Bcl2 oncogenes, J. Nucleic Acids. 2010 (2010), https://doi.org/10.4061/2010/146418

[55] Y. Luo, A. Granzhan, D. Verga, J.-L. Mergny. FRET-MC: A fluorescence melting competition assay for studying G4 structures in vitro, Biopolymers. 112 (2021) e23415. https://doi.org/10.1002/bip.23415

56 M.J. Frisch, G.W. Trucks, H.B. Schlegel, G.E. Scuseria, M.A. Robb, J.R. Cheeseman, G. Scalmani, V. Barone, G.A.Petersson, H. Nakatsuji, et al., Gaussian 16, Revision C.01, Gaussian, Inc.: Wallingford CT, 2019.

57 R.G. Parr, W. Yang. *Density Functional Theory of Atoms and Molecules*; Oxford University Press: New York, 1989. https://doi.org/10.1002/qua.560470107

58 M. E. Casida, Time-Dependent Density Functional Response Theory for Molecules In *Recent Advances in Density Functional Methods*, (1995) 155-192, https://doi.org/10.1142/9789812830586_0005

59 A.W. S. Silva, W.F. Vranken. ACPYPE - AnteChamber PYthon Parser interface. *BMC Research Notes* **2012**, *5*, 367-375, https://doi.org/10.1186/1756-0500-5-367

60 M. Zgarbová, J. Šponer, M. Otyepka, T.E. Cheatham, R. Galindo-Murillo, P. Jurečka, Refinement of the Sugar-Phosphate Backbone Torsion Beta for AMBER Force Fields Improves the Description of Z- and B-DNA. *Chem. Theory Comput.* **2015**, 11, 5723–5736, https://doi.org/10.1021/acs.jctc.5b00716

61 B. Hess, P-LINCS: A Parallel Linear Constraint Solver for Molecular Simulation. J. Chem. Theory Comput., 4 (2008) 116–122, https://doi.org/10.1021/ct700200b

62 M.L. Agazzi, V.A.S. Almodovar, N.S. Gsponer, S. Bertolotti, A.C. Tomé, E.N. Durantini, Diketopyrrolopyrrole-fullerene C60 architectures as highly efficient heavy atom-free photosensitizers: Synthesis, photophysical properties and photodynamic activity. Org. Biomol. Chem., 18 (2020) 1449–1461, https://doi.org/10.1039/C9OB02487E

63 V.A.S. Almodovar, A.C. Tomé, A convenient synthesis of diketopyrrolopyrrole dyes, Molecules, 26 (2021) 4758-2766, https://doi.org/10.3390/molecules26164758

64 L.D. Lavis, R.T. Raines, Bright Building Blocks for Chemical Biology, ACS Chem. Biol., 9 (2014) 855-866, https://doi.org/10.1021/cb500078u

65 Z. Gao, Y. Hao, M. Zheng , Y. Chen, A fluorescent dye with large Stokes shift and high stability: synthesis and application to live cell imaging, RSC Adv. 7 (2017) 7604-7609, https://doi.org/10.1039/C6RA27547H

66 D. Jacquemin, V. Wathelet, E.A. Perpète, C. Adamo, Extensive TD-DFT Benchmark: Singlet-Excited States of Organic Molecules, J. Chem. Theory Comput. 5 (2009) 2420-2435 https://doi.org/10.1021/ct900298e

67 Y. Sun, F. Ji, R. Liu, J. Lin, Q. Xu, C. Gao, Interaction mechanism of 2-aminobenzothiazole with herring sperm DNA, J. Lumin. 132 (2012) 507-512, https://doi.org/10.1016/j.jlumin.2011.09.042

68 S. Bhattacharjee, P.K. Sengupta, S. Bhowmik, Exploring the preferential interaction of quercetin with VEGF promoter G-quadruplex DNA and construction of a pH-dependent DNA-based logic gate, RSC Adv. 7 (2017) 37230-37240, https://doi.org/10.1039/C7RA05930B

69 D.F. Shi, R.T. Wheelhouse, D. Sun, L.H. Hurley, Quadruplex-interactive agents as telomerase inhibitors: Synthesis of porphyrins and structure-activity relationship for the inhibition of telomerase, J. Med. Chem. 44 (2001) 4509-4523, https://pubs.acs.org/doi/10.1021/jm010246u

70 E. Largy, A. Granzhan, F. Hamon *et al.* Visualizing the Quadruplex: From Fluorescent Ligands to Light-Up Probes, Top Curr Chem. 330 (2013) 111-177, https://pubmed.ncbi.nlm.nih.gov/22886708/

[71] J.Q. Hou, S.B. Chen, L.P. Zan, T.M. Ou, J.H. Tan, L.G. Luyt, Z.S. Huang, Identification of a selective G-quadruplex DNA binder using a multistep virtual screening approach, Chem. Commun. 51 (2015) 198-201, https://doi.org/10.1039/C4CC06951J

[72] A. Ali†, M. Bansal, S. Bhattacharya. Ligand 5,10,15,20-Tetra(N-methyl-4-pyridyl)porphine (TMPyP4) Prefers the Parallel Propeller-Type Human Telomeric G-Quadruplex DNA over Its Other Polymorphs. J. Phys. Chem. B. 119 (20151) 5–14 https://doi.org/10.1021/jp505792z

[73] M.I. Umar, D. Ji, C.-Y. Chan, C. K. Kwok. G-Quadruplex-Based Fluorescent Turn-On Ligands and Aptamers: From Development to Applications. Molecules. 24 (2019) 2416. https://doi.org/10.3390/molecules24132416

[74] M.-H. Hu, J. Zhou, W.-H. Luo, S.-B. Chen, Z.-S. Huang, R. Wu, J.-H. Tan. Development of a Smart Fluorescent Sensor That Specifically Recognizes the c-MYC G-Quadruplex. Anal. Chem. 91 (2019) 2480–2487 https://doi.org/10.1021/acs.analchem.8b05298

[75] A. De Rache, J.-L. Mergny, Assessment of selectivity of G-quadruplex ligands via an optimised FRET melting assay, Biochimie. 11 (2015) 194–202, https://doi.org/10.1016/j.biochi.2015.06.002

[76] T. Santos, A. Miranda, M.P.C. Campello, A. Paulo, G. Salgado, E.J. Cabrita, C. Cruz, Recognition of nucleolin through interaction with RNA G-quadruplex, Biochem. Pharmacol. 189 (2020) 114208, https://doi.org/10.1016/j.bcp.2020.114208

[77] A. Ambrus, D. Chen, J. Dai, T. Bialis, R. A. Jones, D. Yang, Human telomeric sequence forms a hybrid-type intramolecular G-quadruplex structure with mixed parallel/antiparallel strands in potassium solution, Nucleic Acids Res., 34 (2006) 2723–2735, https://doi.org/10.1093/nar/gkl348

[78] K. N. Luu, A. T. Phan, V. Kuryavyi, L. Lacroix, D. J. Patel, Structure of the Human Telomere in K+ Solution: An Intramolecular (3 + 1) G-Quadruplex Scaffold, JACS, 128 (2006) 9963-9970 DOI: 10.1021/ja062791w

[79] J. M. Nicoludis, S. P. Barrett, J.-L. Mergny, L. A. Yatsunyk, Interaction of human telomeric DNA with N- methyl mesoporphyrin IX, Nucleic Acids Res. 40 (2012) 5432–5447, https://doi.org/10.1093/nar/gks152

[80] M. P. O'Hagan, J. C. Morales, M. C. Galan, Cover Feature: Binding and Beyond: What Else Can G-Quadruplex Ligands Do?, Eur. J. Org. Chem. (2019) 31-32, https://doi.org/10.1002/ejoc.201901088

[81] B. Jin, X. Zhang, W. Zheng, X. Liu, C. Qi, F. Wang, D. Shangguan, Fluorescence Light-Up Probe for Parallel G-Quadruplexes, Analytical Chemistry 86 (2014), 943-952, https://doi.org/10.1021/ac403676x

[82] A. R. O. Cousins, D. Ritson, P. Sharma, M. F. G. Stevens, J. E. Moses, M. S. Searle, Ligand selectivity in stabilising tandem parallel folded G-quadruplex motifs in human telomeric DNA sequences, Chem. Commun., 50 (2014) 15202-15205

[83] F. D'Aria, B. Pagano, L. Petraccone, C.Giancola, *KRAS* Promoter G-Quadruplexes from Sequences of Different Length: A Physicochemical Study, Int. J. Mol. Sci. **2021**, *22*(1), 448; https://doi.org/10.3390/ijms22010448

84 S. Stump, T. C. Mou, S. R. Sprang, N. R. Natale, H. D. Beall, Crystal structure of the major quadruplex formed in the promoter region of the human c-MYC oncogene, PLoS One. 13 (2018), e0205584 https://journals.plos.org/plosone/article?id=10.1371/journal.pone.0205584

85 A. Ou, J. W. Schmidberger, K. A. Wilson, C. W. Evans, J. A. Hargreaves, M. Grigg, M. L. O'Mara, *et al.*, High resolution crystal structure of a KRAS promoter G-quadruplex reveals a dimer with extensive poly-A π-stacking interactions for small-molecule recognition, Nucleic Acids Res., 48, (2020), 5766–5776, https://doi.org/10.1093/nar/gkaa262

86 J. Marquevielle, C. Robert, O. Lagrabette, M. Wahid, A. Bourdoncle, L.E Xodo, J.-L. Mergny, G. F. Salgado, Structure of two G-quadruplexes in equilibrium in the KRAS promoter, *Nucleic Acids Res.* 16 (2020) 9336–9345, https://doi.org/10.1093/nar/gkaa387

87 S. Cogoi, M. Paramasivam, B. Spolaore, L. E. Xodo, Structural polymorphism within a regulatory element of the human KRAS promoter: formation of G4-DNA recognized by nuclear proteins, Nucleic Acids Research, 36, (2008), 3765–3780, https://doi.org/10.1093/nar/gkn120

88 D. Sun, L. H. Hurley, Biochemical techniques for the characterization of G-quadruplex structures: EMSA, DMS footprinting, and DNA polymerase stop assay, *Methods Mol. Biol.* 608 (2010) 65-79 http://doi: 10.1007/978-1-59745-363-9_5